Spectral methods in general relativity: polarized black holes in AdS space

Miguel Fragoso de Oliveira
Mestrado em Física
Departamento de Física e Astronomia
2013

Orientador
Miguel Sousa Costa, Professor Auxiliar, Faculdade de Ciências da Universade do Porto

Coorientador
João Miguel Augusto Penedones Fernandes, Investigador Auxiliar, Faculdade de Ciências da Universidade do Porto

U.PORTO

FACULDADE DE CIÊNCIAS
UNIVERSIDADE DO PORTO

Todas as correções determinadas pelo júri, e só essas, foram efetuadas.

O Presidente do Júri,

Porto, _____/_____/_____

Acknowledgements

I would like to thank my supervisors, Dr. Miguel Costa and Dr. Joao Penedones, and my colleague Lauren Greenspan, for all their help and support during this project.

Abstract

In this thesis we propose to use spectral methods to find numerical solutions for the Einstein-Maxwell field equations in Anti-de Sitter (AdS) space under the application of an external electric field. We start by introducing spectral methods in non uniform grids, providing a few mathematical examples, and then use them in the physical problem of a steady flow past a fixed cylinder, comparing the results to existing simulations for this problem to a good match.

The main problem about trying to find numerical solutions for the Einstein equations is their general non-ellipticity, and we avoid this problem by introducing the Einstein-de Turck equations. With these, we are able to find both Schwarzschild and Reissner-Nordstrom solutions in an AdS background numerically, and find that they match well with the analytical solutions. We then obtain several black hole solutions with an applied electric field and compute some of their physical properties, such as a breakdown value of the applied electric field at which the black hole either breaks, forming two oppositely charged black holes, or becomes thermodynamically unstable.

Resumo

Neste trabalho, propomos a utilização de métodos espectrais para encontrar solucções numéricas para as equações de campo de Einstein- Maxwell em espaços Anti-de Sitter (AdS), sob a aplicação de um campo eléctrico externo. Começamos por introduzir métodos espectrais em redes não uniformes, dando alguns exemplos matemáticos, para posteriormente os usarmos no problema físico de um fluido bidimensional passando por um cilindro fixo, comparando os resultados com simulações existentes para este problema.

O principal problema em tentar encontrar soluções numéricas para as equações de Einstein é a sua não-elipticidade, e evitamos este problema introduzindo as equações de Einstein-de Turck. Com isto , somos capazes de encontrar numericamente soluções dos tipos Reissner-Nordstrom e Schwarzschild num espaço AdS, e constatar que elas são consistentes com as soluções analíticas existentes. Obtemos então várias soluções do tipo buraco negro com um campo eléctrico aplicado e calculamos algumas das suas propriedades físicas, como por exemplo um valor do campo eléctrico aplicado a partir do qual o buraco negro ou quebra, formando dois buracos negros de carga oposta, ou se torna termodinamicamente instável.

Contents

Chapter 1

Introduction

Physics would be a lot easier if we had the power to solve all of its problems analytically. We could have the behaviour of any physical system described by a finite set of mathematical expressions, and these expressions would make this behaviour easier to visualize.

However, as Einstein himself put it, "God does not care about our mathematical difficulties, He integrates empirically". Indeed, the majority of real life physical problems are simply not soluble by analytical methods alone, specially for complex systems involving several interacting physical processes and when comparing results and observational data. Even conceptually simple physical situations often generate equations for which no known closed-form solution exists, so we are required to use numerical methods in order to achieve a general solution. For example, to find some black hole type solutions of the Einstein-Maxwell equations one needs to tackle the problem numerically, since they are a system of coupled non-linear partial differential equations (PDE).

The power of numerical methods is that they are able to solve these types of problems in a straightforward manner. If we have a physical system governed by a set of equations, we can in principle just plug them into a numerical method of our choice and it will yield a solution. Difficulties may arise when interpreting such solutions, and we must often vary a wide range of parameters just to get a qualitative understanding. Nevertheless, the

solution is able to be found this way. Obviously, one has to be careful when choosing the method for a particular problem, since despite the fact that there may be many that solve that problem with the requested accuracy, the right choice could mean saving a lot of computational time. For example, when solving PDE problems, the character of the equations (elliptic, hyperbolic or parabollic) plays a key role in choosing the appropriate method.

There are a number of such numerical methods, each better suited to a particular type of problem, and in this work we will focus our attention on spectral methods. We will show that they only require a few grid points in the discretization scheme for an outstanding convergence, which allows us to solve highly complex problems with the computational power of a personal laptop.

We will start by giving a brief overview of spectral methods in chapter 2, closely following [27], highlighting their convergence properties, and providing a few examples of their application to boundary value problems. We will then use these methods in physical problems, starting with the well known steady flow of an incompressible fluid past a cylinder in chapter 3, and moving on to the main goal of the project, namely their applications in general relativity, and, in particular, to black holes in AdS space. In chapter 4, we adress the main difficulty usually encountered in trying to compute numerical solutions for the Einstein field equations, their general non-ellipticity, by introducing the Einstein-de Turck equations, to which we will attempt to find numerical solutions in chapter 5.

We chose to work in AdS space for several reasons. First, we can find numerically spherically symmetric solutions and compare them to the exact solutions, Schwarzschild-AdS and Reissner-Nordstrom-AdS, thereby testing the reliability of the method. We also wanted to explore the possibility of polarizing the known black hole solutions. In asymptotically flat space, this can be done with the introduction of a flux tube encasing the black hole, which is like putting the black hole inside a box and applying an electric field through it. The AdS space can be thought to have a potential wall as one approaches asymptotic infinity, hence it is a fancier, more natural box (albeit one with infinite volume). It is therefore easier, both conceptually

and numerically, to study the effects of an external electric field in an AdS background. This will be made clear in chapter 5.

We shall see that the external electric field deforms a neutral black hole to a 'peanut' shape with positive charges accumulating on one side and negative charges accumulating on the other [30]. As we increase the external electric field the deformation increases until a maximum value where we cease to find solutions with S^2 horizon topology. We conjecture that above this maximum value of external electric field the black hole breaks into two separate oppositly charged black holes.

Another motivation to study asymptotically AdS geometries is their dual field theoretic interpretation through AdS/CFT. In particular, the black hole polarization we study in chapter 5 corresponds to the response of a two dimensional spherical material to a space dependent chemical potential that takes a dipolar form on the sphere. We determine the induced charge density distribution as a function of the applied electric field.

Chapter 2

Spectral Methods

In this chapter we propose to introduce and provide examples of the application of spectral methods, which basically consist of discretizing the differential equations of the problem at hand, using non-uniform grids. We also discuss the problems of domains with boundaries and how to specify boundary conditions. Then we generalize these concepts to problems in more than one dimension.

2.1 Definition

As a starting point, we will introduce numerical approximations for the derivative of a function at a point in one dimension. Given a grid of N equidistant points, labeled $\{x_j\}$, with $x_{j+1} = x_j + h$, for all j, the Taylor expansion of a function q around point $x_{j\pm1}$ is given by $q(x_{j\pm1}) = q_{j\pm1} = q(x_j \pm h) \approx q_j \pm q'_j h + q''_j \frac{h^2}{2} + \cdots$ where q_j is the value of the function $q(x)$ at point x_j. Eliminating q_j from both equations yields what is the finite difference approximation for the derivative

$$q'(x_j) = \frac{(q_{j+1} - q_{j-1})}{2h} \tag{2.1}$$

valid up to order h^2.

Looking at the previous expression, it seems the derivative at the boundary points x_0 and x_N is not well defined, however, in boundary value problems

(the ones we will be interested in throughout this project), what happens at these points will be known, determining the values q_0 and q_N. For the moment we can just assume periodic boundary conditions $q_0 = q_N$ and $q_1 = q_{N+1}$. The derivative of a function $q'(x_j) = q'_j = w_j$ can now be represented in matrix form, and in this case its form is very simple, making matrix operations highly efficient.

$$\begin{bmatrix} w_1 \\ \vdots \\ w_N \end{bmatrix} = \frac{1}{2h} D_N^F \begin{bmatrix} q_1 \\ \vdots \\ q_N \end{bmatrix} \tag{2.2}$$

where

$$D_N^F = \begin{bmatrix} 0 & 1 & 0 & & & & -1 \\ -1 & 0 & 1 & & & & \\ 0 & -1 & 0 & & & & \\ & & & \ddots & & & \\ & & & & 0 & 1 & 0 \\ & & & & -1 & 0 & 1 \\ 1 & & & & 0 & -1 & 0 \end{bmatrix}$$

The derivative matrix described uses the value of the function at two different points to approximate its derivative, but it is possible to go beyond that, for example with the use of interpolating functions. The aim is to find the unique polynomial $p_j^{(2)}$ of degree smaller or equal to 2 that satisfies $p_j^{(2)}(x_{j\pm1}) = q_{j\pm1}$ and $p_j^{(2)}(x_j) = q_j$, and then take $q'_j = p_j^{(2)\prime}(x_j)$.

The interpolating function that obeys the required conditions is given by

$$p_j^{(2)}(x) = q_{j-1}\frac{(x-x_j)(x-x_{j+1})}{2h^2} - q_j\frac{(x-x_{j-1})(x-x_{j+1})}{h^2} + \\ + q_{j+1}\frac{(x-x_j)(x-x_{j-1})}{2h^2} \tag{2.3}$$

Our approximation for the derivative $p^{(2)\prime}_j(x_j)$ precisely matches equation 2.1.

To go further, we can increase the number of points on which to impose the value of the function, thereby increasing the degree of the interpolating polynomial, for a more accurate estimate of the derivative. For example,

considering the fourth-order analogue of $p_j^{(2)}$, a polynomial $p_j^{(4)}$ for which $p_j^{(4)}(x_{j\pm2}) = q_{j\pm2}$, $p_j^{(4)}(x_{j\pm1}) = q_{j\pm1}$ and $p_j^{(4)}(x_j) = q_j$, the derivative is approximated as follows

$$q'_j = \frac{1}{12h}(q_{j-2} - 8q_{j-1} + 8q_{j+1} - q_{j+2}) \tag{2.4}$$

The principle behind spectral methods is to take the limit where the degree of this polynomial goes to infinity, in which case the derivative of the function at a single point depends on the values of the function at all points. In practice this is impossible, since we have to work with a finite grid of points. So, we take p to be a single function, independent of j, such that $p(x_j) = q_j$ for all values of j and then take $q'_j = p'(x_j)$. This way, the derivative matrix will be more dense, and more difficult to work with, since the derivative at a point will depend on the function value at all points in the grid, but also the number of points required for the same level of convergence will be significantly smaller. Different choices of grids can result in different functions $p(x)$, and more than one function can give the same convergence properties.

It would seem that the most straightforward idea is to use an equidistant grid of $(N+1)$ points, but that turns out not to be the case for all functions, because of Runge's phenomenon, a problem that occurs when we use high degree polynomials to interpolate some functions on equidistant grids. The plot shown in Figure 2.1 represents the case of the Runge function $f(x) = \frac{1}{1+25x^2}$ for $x \in [-1, 1]$, for which this phenomenon is clear.

At the interpolating points, the error between the function and the interpolating polynomial is (by definition) zero. Between the interpolating points (especially in the region close to the endpoints, the error between the function and the interpolating polynomial gets worse for higher-order polynomials (or higher number of points in the grid). In order to analyze this effect, consider the Weierstrass approximation theorem, stating that every continuous function $f(x)$ defined on an interval $[a, b]$ can be uniformly approximated as closely as desired by a polynomial function $P_n(x)$ of sufficiently large degree lesser or equal to n, with an interpolation error $\epsilon_n = \max_{a\leq x\leq b}|f(x) - P_n(x)|$

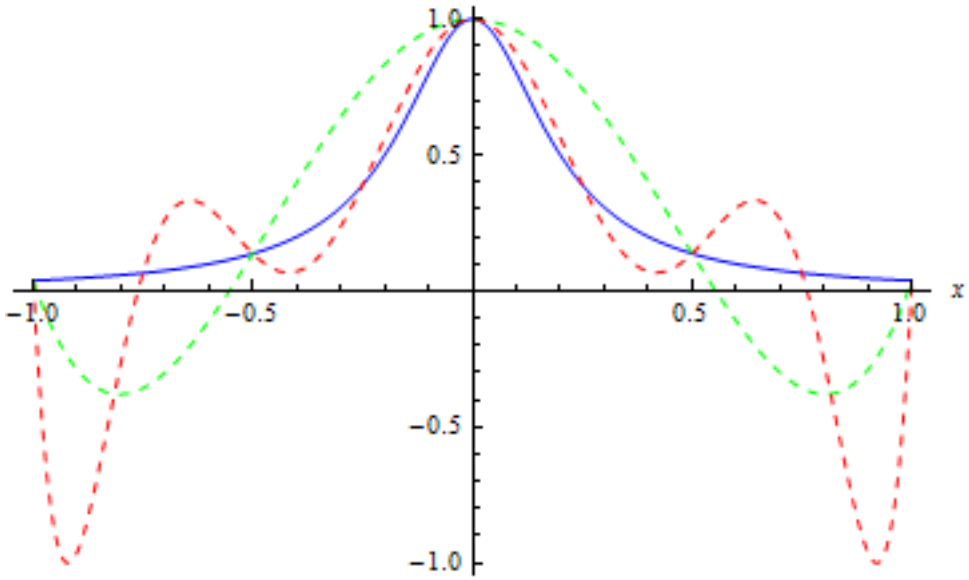

Figure 2.1: The blue line represents the function f, the dashed lines are the interpolating polynomial of degree 4 (red) and 8 (green) on an evenly spaced grid.

that goes to zero as n goes to infinity

$$\lim_{n\to\infty}\left(\max_{a\le x\le b}|f(x)-P_n(x)|\right)=0 \tag{2.5}$$

Taking our example of the Runge function, and a set of points given by $x_i = \frac{2i}{n}-1$ with a polynomial $P_n(x)$, the resulting interpolation error $\max_x|f(x)-P_n(x)|$ increases without bound as the degree of the polynomial is increased, as shown by the logarithmic plot in Figure 2.2. So, using this grid,

$$\lim_{n\to\infty}\left(\max_{a\le x\le b}|f(x)-P_n(x)|\right)\to\infty$$

The correct approach is to change from the uniform grid to another type of grid where convergence is guaranteed. Since the convergence problems arise near the boundaries, the oscillations can be minimized by using nodes that are distributed more densely towards the edges of the interval, with asymptotic density (on the interval $[-1,1]$) given by $d(x)\approx 1/\sqrt{1-x^2}$ [8]. This property will also be very useful when dealing with boundary value problems, where the method needs to be very accurate near these crucial

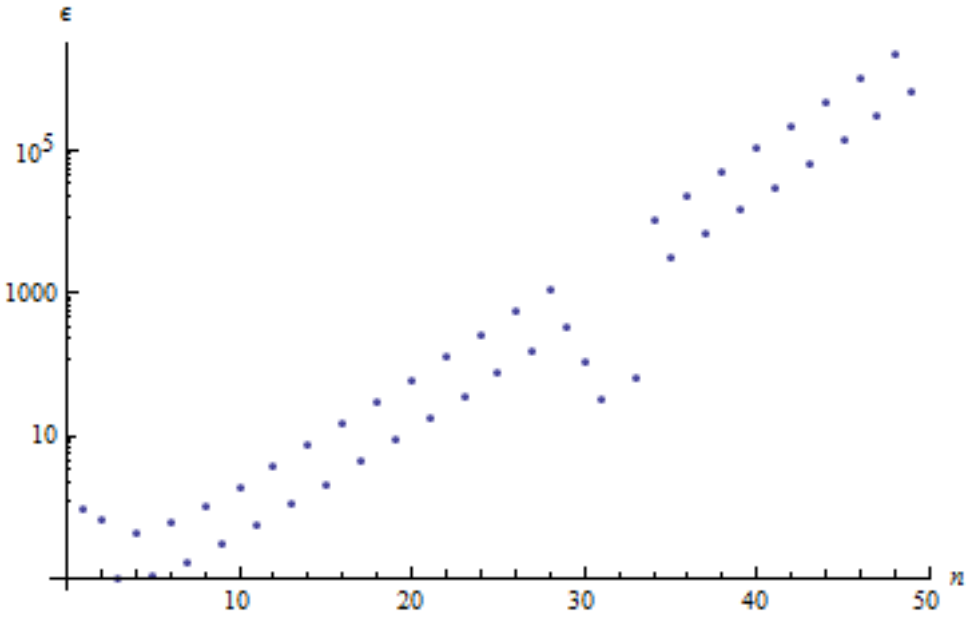

Figure 2.2: Interpolation error ϵ_n of $f(x)$ as a function of the degree n of the interpolating polynomial, determined using an evenly spaced grid

points. Specifically, the set of points known as the Chebyshev points are the ones that minimize the interpolation error ϵ_n [18]

$$x_j = \frac{a+b}{2} + \frac{a-b}{2} \cos \frac{\pi j}{n}$$

To show the difference between spectral methods on evenly spaced and Chebyshev grids, we show in Figure 2.3 the interpolation function obtained using this set of points (with $a = -b = 1$), as well as the interpolation error in Figure 2.4. In this case, the function is much better approximated and the error decreases exponentially as n goes to infinity.

2.2 Chebyshev differentiation matrices

Now that we have introduced a set of points on which to discretize our problem, we are going to determine the matrices of differentiation that act on the grid point values of the functions, used to obtain the discretized versions of the equations used in spectral methods.

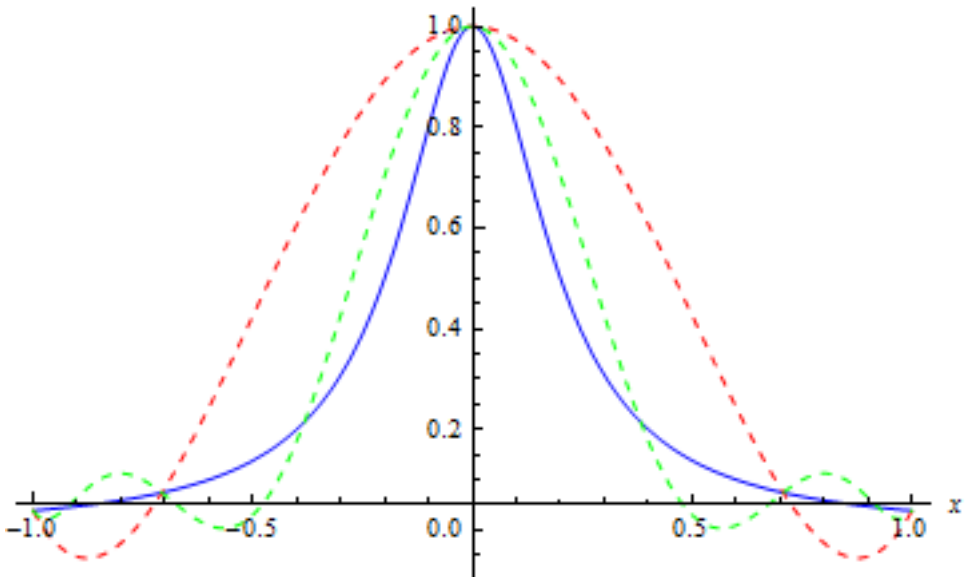

Figure 2.3: The blue line represents the function f, the dashed lines are the interpolating polynomial of degree 4 (red) and 8 (green) on a Chebyshev grid. The oscillatory problems near the boundaries seen in Figure 2.1 no longer occur using this grid.

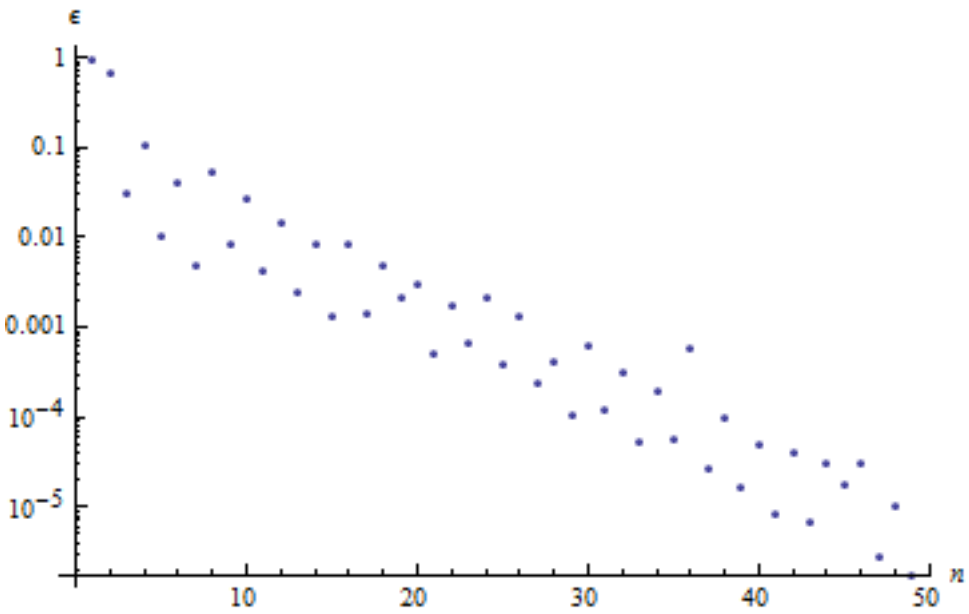

Figure 2.4: Interpolation error ϵ_n of $f(x)$ as a function of the degree n of the interpolating polynomial, determined using a Chebyshev grid

This operation is linear on the values of q_j, as we will exemplify for the $N = 1, 2$ case. Therefore, we can write the differentiation operation as an $(N + 1) \times (N + 1)$ matrix, denoted here by D_N, acting on a vector composed of the q_j which we will denote by $\vec{q}_N$. The grid point values of the derivative will be denoted by w_j, so the equation for the differentiation becomes $\vec{w}_N = D_N.\vec{q}_N$. Let us turn to the examples of $N = 1, 2$ before proceeding to the more general case.

If $N = 1$, the grid points are just $x_0 = 1$, $x_1 = -1$, and the values of the functions at these points are represented by q_0 and q_1. The interpolation polynomial and its derivative are

$$p_1(x) = \frac{1}{2}\left((x + 1)q_0 + (1 - x)q_1\right) \tag{2.6}$$

$$p_1'(x) = \frac{1}{2}(q_0 - q_1) \tag{2.7}$$

The differentiation matrix acting on the vector $\vec{q}_1 = (q_0, q_1)^T$ is then

$$D_1 = \begin{bmatrix} \frac{1}{2} & -\frac{1}{2} \\ \frac{1}{2} & -\frac{1}{2} \end{bmatrix} \tag{2.8}$$

In the case of $N = 2$, the interpolation points are $x_0 = 1$, $x_1 = 0$ and $x_2 = -1$, and the interpolation polynomial $p_2(x)$ is given by

$$p_2(x) = \frac{1}{2}x(1 + x)q_0 + (1 + x)(1 - x)q_1 + \frac{1}{2}x(1 - x)q_2 \tag{2.9}$$

The approximation for the derivative is now a linear polynomial of the form

$$p_2'(x) = (x + \frac{1}{2})q_0 - 2xq_1 + (x - \frac{1}{2})q_2 \tag{2.10}$$

Evaluating equation 2.10 at each interpolation point and reading the coefficients of q_0, q_1 and q_2 we obtain the differentiation matrix

$$D_2 = \begin{bmatrix} \frac{3}{2} & -2 & -\frac{1}{2} \\ \frac{1}{2} & 0 & -\frac{1}{2} \\ -\frac{1}{2} & 2 & -\frac{3}{2} \end{bmatrix} \tag{2.11}$$

Generally, an interpolating polynomial of degree N, interpolating $(N+1)$ data points, $p_N(x)$, is given by the linear combination

$$p_N(x) = \sum_{j=0}^{N} q_j l_j(x) \tag{2.12}$$

where

$$l_j(x) = \prod_{p=0;p\neq j}^{N} \frac{(x - x_p)}{(x_j - x_p)} \tag{2.13}$$

To determine the general form of the differentiation matrix, we need to take the derivative of the interpolating polynomial, obtaining

$$l_i'(x) = l_i(x) \sum_{j=0;j\neq i}^{N} \frac{1}{x - x_j} \tag{2.14}$$

So, this matrix is simply

$$(D_N)_{ki} = l_i'(x_k) = l_i(x_k) \sum_{j=0;j\neq i}^{N} \frac{1}{x_k - x_j} \tag{2.15}$$

We can use this simple formula to determine the specific form of the entries of the matrix for each N with any grid.

In the case of the Chebyshev grid, the entries of the $(N+1) \times (N+1)$ spectral differentiation matrix are

$$\begin{aligned} (D_N)_{00} &= -(D_N)_{NN} = \frac{2N^2+1}{6} \\ (D_N)_{ii} &= -\frac{x_i}{2(1-x_i^2)}, \qquad i \in \{1, \cdots, N-1\} \\ (D_N)_{ij} &= \frac{c_i}{c_j} \frac{(-1)^{i+j}}{x_i - x_j}, \qquad i \neq j \end{aligned} \tag{2.16}$$

where

$$c_i = \begin{cases} 2 & i = 0, N \\ 1 & \text{otherwise} \end{cases}$$

As was previously noted, because of the fact that this method uses all grid points to determine the derivatives at a given point, these matrices will be

denser than the ones used in, for example, finite differences, so they will result in more complicated numerics when dealing with operations where they appear. However, this method has a rate of convergence that is exponential with the number of points considered, thus we only need to consider a few of these points, in which case matrix operations, even the ones where they are very dense, are not that complicated to perform.

2.3 Generalization to two dimensions

The method developed so far allows us to work with differential equations for functions q(x) dependent on one parameter only, but it can be generalized to higher dimensions, PDEs of the form $E[q(x,y), \partial_x q, \partial_y q, \dots] = 0$. To start, we need a two-dimensional grid, and we can just use the Chebyshev grid in each direction independently. The points of this grid, with each increase in dimensionality of the system, become more clustered at its boundaries.

To generalize the Chebyshev spectral differentiation matrices we are going to use a particular case of tensor product, the Kronecker product, denoted by $A \otimes B$, which transforms two matrices A and B with dimensions $n_A \times m_A$ and $n_B \times m_B$ into a new matrix with dimensions $n_A n_B \times m_A m_B$, like in the following example.

$$\begin{bmatrix} a_{11} & a_{12} \\ a_{21} & a_{22} \end{bmatrix} \otimes \begin{bmatrix} b_{11} & b_{12} \\ b_{21} & b_{22} \end{bmatrix} = \begin{bmatrix} a_{11}b_{11} & a_{11}b_{12} & a_{12}b_{11} & a_{12}b_{12} \\ a_{11}b_{21} & a_{11}b_{22} & a_{12}b_{21} & a_{12}b_{22} \\ a_{21}b_{11} & a_{21}b_{12} & a_{22}b_{11} & a_{22}b_{12} \\ a_{21}b_{21} & a_{21}b_{22} & a_{22}b_{21} & a_{22}b_{22} \end{bmatrix} \tag{2.17}$$

We can consider $N = 2$ and try to construct the two-dimensional Chebyshev differentiation matrices in this very simple case. We start by indexing the points on the grid (x_i, y_j) with a single number k, ranging from 1 to $(N+1)^2$, ordering them up to down and right to left with $k = (i-1)(N+1) + j$.

We also label the values of the functions at the points in the grid and organize them in a vector $q = \{q_1, \cdots, q_9\}^T$.

We want to approximate the partial derivative along one of the directions

while ignoring what happens in the remaining direction. Let I_3 denote the 3×3 identity matrix and D_2 the differentiation matrix constructed in the previous section, then the derivative along y can be determined by taking the Kronecker product $D_2 \otimes I_3$, and the derivative along x by $I_3 \otimes D_2$. Their explicit forms are given in equations 2.18 and 2.19.

$$D_y^{(2)} = \begin{bmatrix} \frac{3}{2} & -2 & \frac{1}{2} & 0 & 0 & 0 & 0 & 0 & 0 \\ \frac{1}{2} & 0 & -\frac{1}{2} & 0 & 0 & 0 & 0 & 0 & 0 \\ -\frac{1}{2} & 2 & -\frac{3}{2} & 0 & 0 & 0 & 0 & 0 & 0 \\ 0 & 0 & 0 & \frac{3}{2} & -2 & \frac{1}{2} & 0 & 0 & 0 \\ 0 & 0 & 0 & \frac{1}{2} & 0 & -\frac{1}{2} & 0 & 0 & 0 \\ 0 & 0 & 0 & -\frac{1}{2} & 2 & -\frac{3}{2} & 0 & 0 & 0 \\ 0 & 0 & 0 & 0 & 0 & 0 & \frac{3}{2} & -2 & \frac{1}{2} \\ 0 & 0 & 0 & 0 & 0 & 0 & \frac{1}{2} & 0 & -\frac{1}{2} \\ 0 & 0 & 0 & 0 & 0 & 0 & -\frac{1}{2} & 2 & -\frac{3}{2} \end{bmatrix} \tag{2.18}$$

$$D_x^{(2)} = \begin{bmatrix} \frac{3}{2} & 0 & 0 & -2 & 0 & 0 & \frac{1}{2} & 0 & 0 \\ 0 & \frac{3}{2} & 0 & 0 & -2 & 0 & 0 & \frac{1}{2} & 0 \\ 0 & 0 & \frac{3}{2} & 0 & 0 & -2 & 0 & 0 & \frac{1}{2} \\ \frac{1}{2} & 0 & 0 & 0 & 0 & 0 & -\frac{1}{2} & 0 & 0 \\ 0 & \frac{1}{2} & 0 & 0 & 0 & 0 & 0 & -\frac{1}{2} & 0 \\ 0 & 0 & \frac{1}{2} & 0 & 0 & 0 & 0 & 0 & -\frac{1}{2} \\ -\frac{1}{2} & 0 & 0 & 2 & 0 & 0 & -\frac{3}{2} & 0 & 0 \\ 0 & -\frac{1}{2} & 0 & 0 & 2 & 0 & 0 & -\frac{3}{2} & 0 \\ 0 & 0 & -\frac{1}{2} & 0 & 0 & 2 & 0 & 0 & -\frac{3}{2} \end{bmatrix} \tag{2.19}$$

2.4 Boundary value problems

In this section we will present some examples of how to use the method developed so far to solve boundary value problems. We will start with a simple problem involving fixed value boundary conditions (Dirichlet), then proceed to more complicated choices such as Neumann boundary condition, where the value of the derivative is specified, and Robin boundary condition,

where a linear combination of the values of the function and the values of its derivative at the boundaries is provideds.

As an example, take the following non-linear differential equation

$$q_{xx}(x) = e^{\frac{q(x)}{2}}, \qquad x \in [-1, 1] \tag{2.20}$$

where we are using the standard PDE notation $q_x = \partial_x q$.

This equation admits the following general solution

$$q(x) = 4 \log \left(\frac{2A}{\cos\left[A(x+B)\right]} \right) \tag{2.21}$$

where the integration constants A and B are to be fixed by our choice of boundary conditions.

We will start by considering the Dirichlet boundary conditions $q(\pm 1) = 0$. For this particular case, the analytical solution is given by $B = 0$ and A equal to the solution of the equation $2A = \cos A$, which yields $A \approx 0.45$. We want to find this solution numerically with the use of spectral methods in a Chebyshev grid. In order to do this, we start by putting our equation into the form $E[q_{xx}, q_x, q] = 0$, as in

$$E[q_{xx}, q_x, q] = q_{xx}(x) - e^{\frac{q(x)}{2}} \tag{2.22}$$

Now, we discretize E at each point of our grid $\{x_j\}$, $j \in \{1, \cdots, N+1\}$, and name it E_j. The function is approximated by a vector q whose entries are the values of the functions at each point x_j, $q_j = q(x_j)$. Derivatives are approximated by acting with the differentiation matrices defined in the previous section. So, in the case of the considered equation, the approximation for E at each point on the grid is given by

$$E_i = (D_N^2)_{ij} q_j - e^{\frac{q_i}{2}} \tag{2.23}$$

where $D_N^2 = D_N . D_N$.

To find the solution of $E_i = 0$ at each point on the grid, we will use an iterative process, to which we give an initial guess for the seed solution $q_i^{(0)}$,

and the process iterates it to the true solution, up to a given precision.

The method we used to solve these equations was the Newton method, based on the expansion of E_i around q_j, which assumes we can make an initial guess and then determine corrections to it in such a way that they approximate q_i from the correct solution. This expansion is given by

$$0 = E_i[q_j + \delta q_j] \approx E_i[q_j] + \left(\frac{\partial E_i}{\partial q_j}\right)\delta q_j \implies A_{ij}\delta q_j = -E_i[q_j] \tag{2.24}$$

where

$$A_{ij} = \frac{\partial E_i}{\partial q_j} \tag{2.25}$$

In this method, we make an assumption for the initial solution, namely $q_i^{(0)}$, then compute A_{ij} and determine δq_i, then setting $q_i^{(1)} = q_i^{(0)} + \delta q_i$ and repeating this process until the required convergence is reached.

However, at the boundaries, we are not interested in solving the equations. Instead, we impose conditions that constrain the value of the solution, these boundary conditions can be seen as equations imposed at the points x_1 and x_{N+1}, as in

$$\begin{aligned} E_i &= q_i - a, \quad i = 1 \\ E_i &= q_i - b, \quad i = N+1 \end{aligned} \tag{2.26}$$

for any Dirichlet type condition where $q(x_1) = a$ and $q(x_{N+1}) = b$. In this case $a = b = 0$ so the first and last conditions are just $E_1 = q_1$ and $E_{N+1} = q_{N+1}$. So, if we just choose a seed $q_i^{(0)} = 0$, these conditions will automatically be satisfied and we will have to solve

$$A_{\alpha\beta}\delta q_\beta = -E_\alpha, \quad \alpha, \beta \in \{2, \ldots, N\} \tag{2.27}$$

In the first step, we will calculate (A) and E using the seed solution, obtaining a new solution, and then using it to determine new values for (A) and E, up until the solution reaches the desired accuracy $||\vec{q}^{(n+1)} - \vec{q}^{(n)}|| \leq \epsilon$. Working in a grid with $N = 16$, we reach convergence for $\epsilon = 10^{-12}$ after only 3 iterations. The solution is plotted in Figure 2.5.

This example was somewhat trivial, since the boundary conditions are

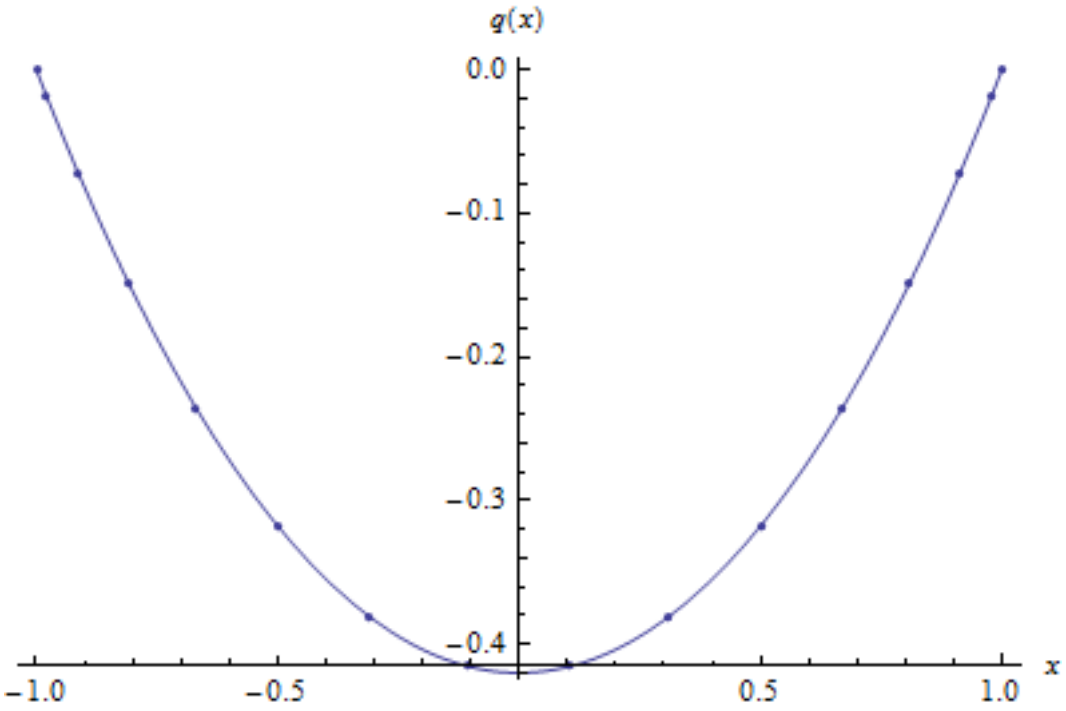

Figure 2.5: Exact (solid line) and numerical (dots) solution of equation 2.20, subject to $q(\pm 1) = 0$.

linear and the solution can be proven to be unique. Let us try to solve the same differential equation 2.20, but now subject to the following non-linear boundary conditions

$$q(-1) = 0 \quad \text{and} \quad q'(1) = e^{q(1)} - 1 \tag{2.28}$$

In this case, we have two real analytical solutions, corresponding to $\{A, B\} \approx \{0.48, 0.47\}$ and $\{A, B\} \approx \{0.11, -11.23\}$. The question arises as how to distinguish the two solutions. The answer to this relies on our choice of seed solution $q_i^{(0)}$. To implement these boundary conditions, we still take $E_{N+1} = q_{N+1}$, but now we take

$$E_1 = (D_N)_{1j} q_j - e^{q_0} + 1 \tag{2.29}$$

The steps the program will take are exactly the same, and now convergence is achieved after 7 iterations, for $N = 16$, and the result obtained using

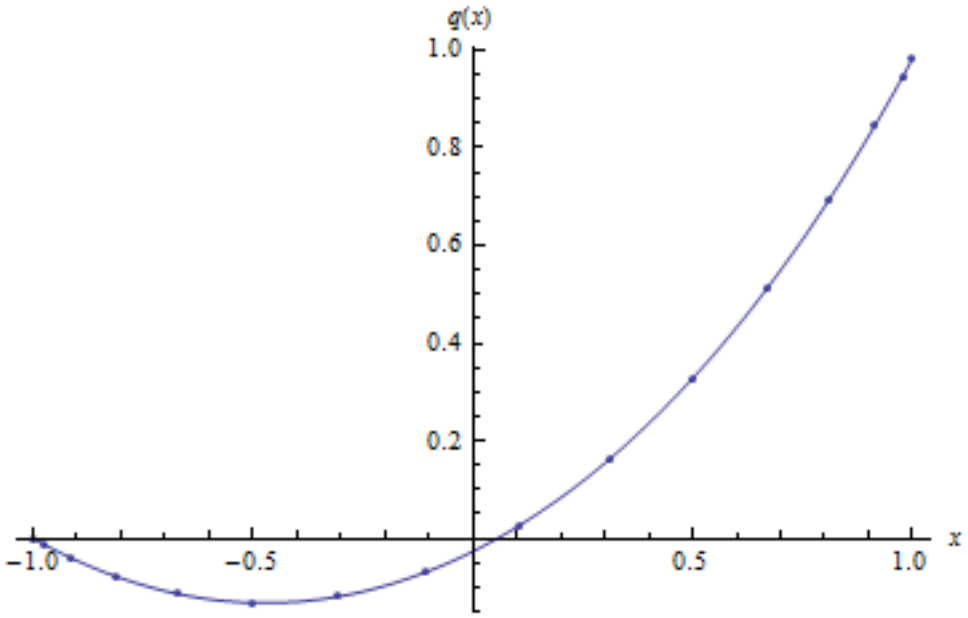

Figure 2.6: Exact (solid line) and numerical (dots) solution of equation 2.20, subject to 2.28. Seed solution $q^{(0)} = \{0, \ldots, 0\}$.

$q^{(0)} = \{0, \ldots, 0\}$ is plotted in Figure 2.6.

If we start with $q^{(0)} = -\{1, \ldots, 1\}$, the solution after 5 iterations is represented in Figure 2.7, and the numerical results are again in remarkable agreement with the analytical ones.

As we have seen in the previous section, the differentiation matrices generalize easily into two dimensions. The same holds true for this method and the problem of imposing boundary conditions. We will go into more detail about this in the next chapter. Finally, another possible generalization is when we want to consider a system of M differential equations for a set of M functions. In this case, instead of considering the discrete version of a single equation, namely E_i, we should consider the discrete version of the system, for which we need to introduce another index α, ranging from 1 to M, and replacing E_i by E_i^α and q_i by q_i^α. The method presented in this section then follows automatically.

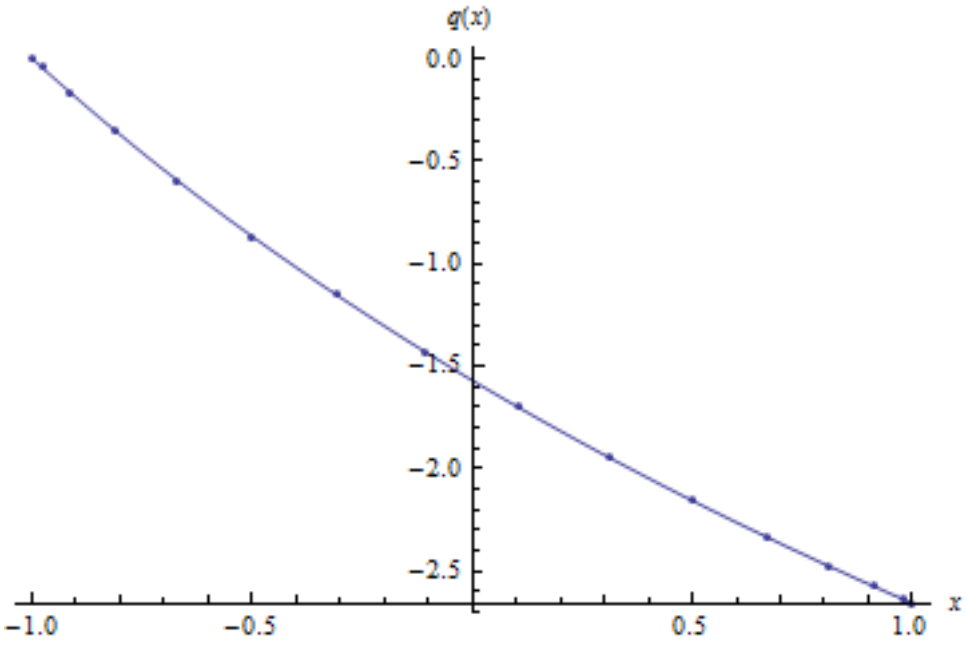

Figure 2.7: Exact (solid line) and numerical (dots) solution of equation 2.20, subject to 2.28. Seed solution $q^{(0)} = -\{1, \ldots, 1\}$.

2.5 Conclusion

In this chapter we have introduced the spectral methods and seen how they can be an extremely powerful tool in the problem of numerically solving differential equations. However, a suitable grid has to be chosen, at the risk of leading to high numerical instabilities such as the Runge phenomenon. We have shown that there is a grid that works extremely well in overcoming this phenomenon, the Chebyshev grid.

We further deduced the general form of the differentiation matrix in spectral methods, and its exact form for the Chebyshev grid. We also generalized their construction to higher dimensions.

Finally, we have seen, with a few examples, how to use these methods to solve boundary value problems involving differential equations, with both linear and non-linear boundary conditions. In all the examples the agreement between numerical and analytical results was better than 10^{-12} with only a few iterations and no more than 16 points in the grid, showing just how powerful these methods can be. These boundary value problems must,

however, be in an elliptic form in order for the initial data to be well-defined everywhere, in contrast with other methods where we want the problem to have an hyperbolic character (for example, wave propagation) in order to describe its dynamics.

In the following chapters we will present numerical applications of spectral methods to a number of physical contexts.

Chapter 3

Flow past a cylinder

As an introduction to the two-dimensional problem, we will start with a problem that has been thoroughly studied, the steady flow of an incompressible fluid past a solid cylinder (see Fig. 3.1) in two dimensions.

3.1 Navier-Stokes equations

The Navier-Stokes equations are used to describe the motion of fluid-like substances. Their solutions, unlike in classical mechanics where solutions typically determine the position or trajectory of a particle, determine the velocity field of the fluid considered, and once they are solved, other quantities of interest can be found, such as flow rate or drag.

In general, they are a system of nonlinear partial differential equations, but in some cases (such as creeping or Stokes flow) some assumptions are made that simplify the equations to linear equations, allowing for an analytical solution. However, most real problems using these equations are made very difficult or impossible to solve by the nonlinearity, which is the main contributor to turbulence, or time dependent chaotic behaviour seen in many fluid flows, that the equations model. For the purpose of our work, these issues will be ignored, so an adequate choice of parameters will have to be made in the next section.

In an inertial frame of reference, the general form of the Navier-Stokes

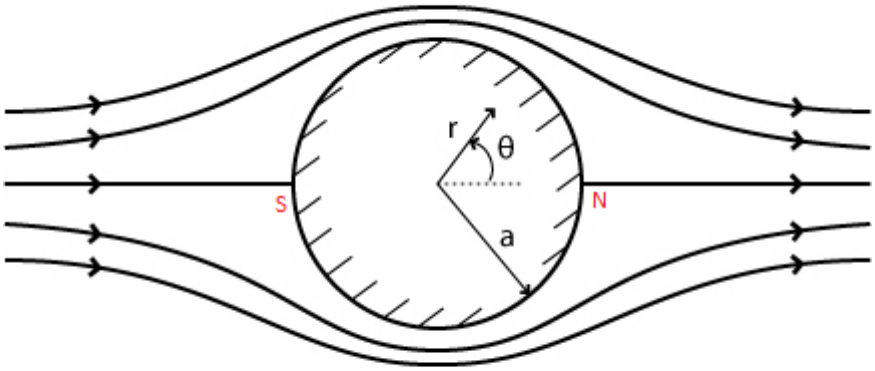

Figure 3.1: Diagramatic representation of a steady flow past a cylinder.

equations of fluid motion is [13]

$$\vec{a} = \left(\frac{\partial \vec{u}}{\partial t} + \vec{u}.\nabla\vec{u}\right) = \vec{g} - \frac{1}{\rho}\nabla p + \frac{\xi + \eta/3}{\rho}\nabla(\nabla.\vec{u}) + \frac{\eta}{\rho}\Delta\vec{u} \qquad (3.1)$$

where $\vec{u}$ represents the velocity field of the fluid, $\vec{g}$ the acceleration due to gravity, p the pressure field, ρ the fluid's density, and ξ and η are parameters related to the dynamical viscosity of the fluid.

The left hand side of this equation represents the acceleration of the fluid, both from time dependent velocity and from convective acceleration, a nonlinear effect which is due to the spatial dependency of the velocity field. In the case of creeping flow the convective part of the acceleration is disregarded.

The right hand side contains the forces acting on the fluid, be it gravity or any form of stress. Obviously, an extra term could be added if any external forces were present (like a pump). The effect of the pressure gradient on the flow is to accelerate the fluid in the direction from high pressure to low pressure.

Throughout this project we will only consider stationary incompressible

fluids, that is, fluids obbeying the conditions $\nabla.\vec{v} = 0$ and $\frac{\partial \vec{v}}{\partial t} = 0$, with constant viscosity. We will also neglect the action of gravity. Using these assumptions, the Navier-Stokes equations become

$$\vec{a} = \vec{v}.\nabla\vec{v} = -\frac{1}{\rho}\nabla p + \frac{\eta}{\rho}\Delta\vec{v} \tag{3.2}$$

Another way to simplify the problem is to make these equations dimensionless, multiplying the previous equation by $\frac{L}{\rho v_0^2}$, where L is a characteristic length scale of the system and v_0 is a characteristic velocity of to the fluid. If we set

$$\vec{v}' = \frac{\vec{v}}{v_0}, \quad p' = \frac{p}{\rho v_0^2}, \quad \nabla' = L\nabla \tag{3.3}$$

Substituting 3.3 into equation 3.2, we obtain its nondimensional version, with only one parameter to tune, the Reynold's parameter $Re = \lambda^{-1} = \frac{\rho L v_0}{\eta}$. Dropping the primes, the equation becomes

$$\vec{a} = \vec{v}.\nabla\vec{v} = -\nabla p + \lambda\Delta\vec{v} \tag{3.4}$$

Note that, as $\lambda \to 0$, the viscous term vanishes, and the flow is approximately inviscid.

3.2 Boundary conditions and coordinates

We want to consider a problem when the fluid is flowing (in the x-direction) past a cylinder of radius R, fixed at the origin of the coordinates. Since we fixed the cylinder, the velocity of the fluid at the surface of the cylinder should be zero $\vec{u}(x, y) = 0, \;\; x^2 + y^2 + z^2 = R^2$. Besides, we take the velocity of the fluid at infinity to be equal to a characteristic velocity $u_\infty \vec{e}_x$, since the finite size of the cylinder means that it will only noticeably influence the behaviour of the fluid up to a given radius.

Additionally, since there is a symmetry in relation to the $x = 0$ axis (or to $\theta = 0, \pi$), the y component of the velocity should vanish at these boundaries (poles). Finally, regarding the pressure, as previously noted its value at infinity is irrelevant to our problem, so we can just set it to zero,

and the normal component of the gradient of the pressure should also go to zero at the surface of the cylinder.

We take the characteristic length scale of the problem to be the radius of the cylinder $L = R$, and the average velocity to be the velocity at infinity, so $u_0 = u_\infty$.

We then introduce new coordinates for the problem, in order to introduce a grid

$$\begin{aligned} v &= 1 - \frac{2R}{\sqrt{x^2+y^2}} = 1 - \frac{2R}{r} \\ w &= \frac{2}{\pi}\arctan\left(\frac{y}{x}\right) - 1 = \frac{2}{\pi}\theta - 1 \end{aligned} \tag{3.5}$$

as we can see, $w, v \in [-1, 1]$. The inverse relations are given by

$$\begin{aligned} x &= -\frac{2R}{1-v}\sin\left(\frac{\pi}{2}w\right) \\ y &= \frac{2R}{1-v}\cos\left(\frac{\pi}{2}w\right) \end{aligned} \tag{3.6}$$

With equations 3.4 and the equation for an incompressible fluid

$$div\ \vec{u} = 0 \tag{3.7}$$

we have three equations for three unknown functions $u_x(v, w)$, $u_y(v, w)$ and $p(v, w)$. Note that, while we change coordinates in the problem, we do not change the components of the velocity field, instead leaving them as two independent functions.

In terms of boundary conditions (see Figure 3.2), at the surface of the sphere, as we have mentioned, the velocity vanishes, as well as the gradient of the pressure; at infinity the velocity returns to its characteristic value $\vec{u}_\infty$, meaning $u_x = u_0$ and $u_y = 0$, while the pressure has a value p_0 which is irrelevant to our problem; and at the poles u_y vanishes, while u_x and p obey

$$\frac{\partial p}{\partial w}|_{w=\pm 1} = 0 \tag{3.8}$$

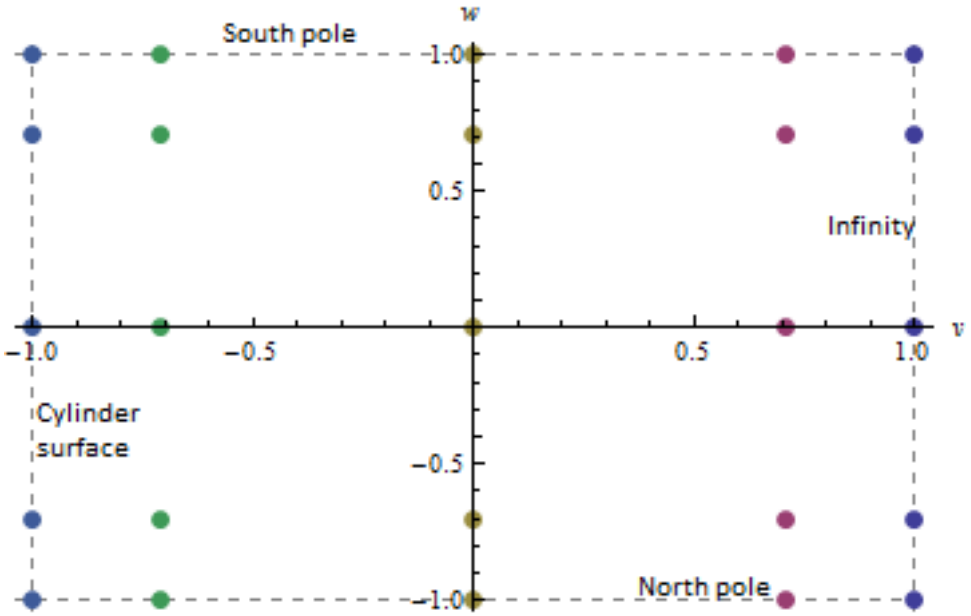

Figure 3.2: Chebyshev grid in (v, w) coordinates.

and

$$\frac{\partial u_x}{\partial w}|_{w=\pm 1} = 0 \tag{3.9}$$

3.3 Spectral Method

With the coordinates introduced in the previous section, we can discretize the problem using a Chebyshev grid for both the w and v directions.

$$\begin{aligned} v_i &= \cos\left(\frac{\pi i}{n}\right), \quad i \in \{0, \ldots, n\} \\ w_j &= \cos\left(\frac{\pi j}{n}\right), \quad j \in \{0, \ldots, n\} \end{aligned} \tag{3.10}$$

In Figure 3.2 we present this grid in (v, w) coordinates and in Figure 3.3 in (x, y) for $N = 25$ points, so it can be seen exactly what points are being used to interpolate the functions. The usefulness of this grid is extremely obvious there, since there is clustering of points near the cylinder, which is exactly where the behaviour of the fluid changes more rapidly and where we don't know what will happen, and just a few points away from the cylinder, where

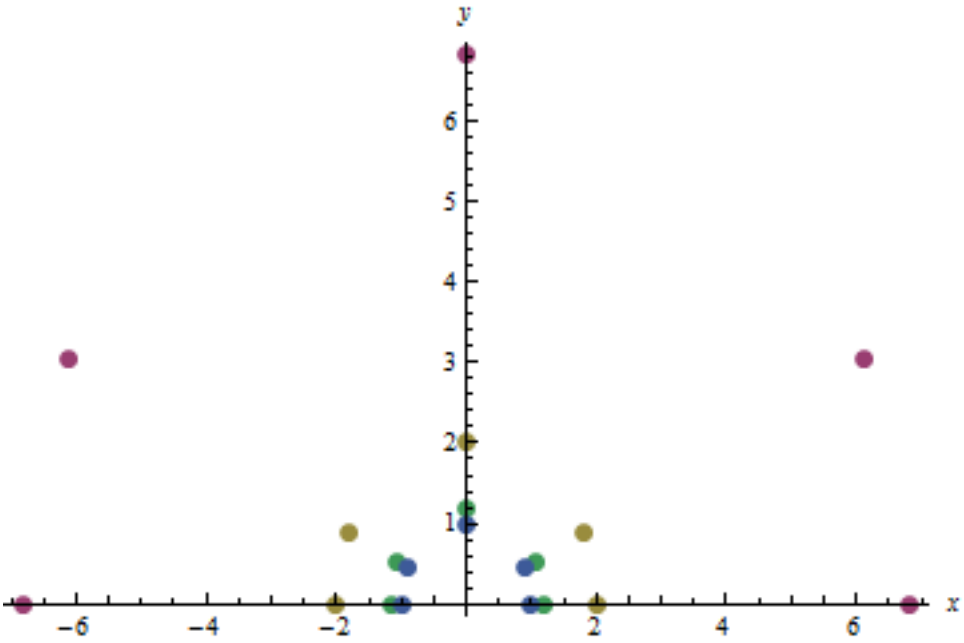

Figure 3.3: Chebyshev grid in (x, y) coordinates. Note that there are 5 points at infinity ($v = 1$) that are not represented.

it is intuitively obvious that the flow will be more or less homogeneous.

We can aggregate the points of the grid in a two dimensional table where each point can be defined by a pair $(i, j) \in \{1, \ldots, n+1\}$. In order to simplify the method, we wish to introduce an index to identify each point with only one value k, such as

$$k = (i - 1)(n + 1) + j \tag{3.11}$$

Now we will discretize the problem, changing all instances of the functions u_x, u_y and p to some lists $q_x = \{q_{x_1}, \ldots, q_{x_{n+1}}\}$, $q_y = \{q_{y_1}, \ldots, q_{y_{n+1}}\}$ and $p = \{p_1, \ldots, p_{n+1}\}$, where q_i represents the value of the function q at the point of index i. Also, the two dimensional differentiation matrices we determined in section 2.3 will be used as ∂_v and ∂_w. The equations 3.4 and 3.7 then become discretized, and we can apply them separately at each point in the grid, remembering to also impose the boundary conditions 3.8 and 3.9 at the points in the boundaries, in the way mentioned in the previous chapter.

After having these equations at all points, we can proceed to solve them using the Newton method. In this case we have three equations, so we label

them $E^{(\alpha)}$, $\alpha = \{1, 2, 3\}$. We can use the method exactly in the same way as in section 2.4, if we create a list E of length $3N$ (where N is the total number of points) where the first N values are those of $E^{(1)}$, the second N those of $E^{(2)}$ and tha last N values are those of $E^{(3)}$. We can also join the lists of function values as $q = \{q_x, q_y, p\}$, also of length 3N. To compute A_{ij} we first determine $(A^{(1)})$, $(A^{(2)})$ and $(A^{(3)})$ by

$$A_{ij}^{(1)} = \frac{\partial E_i}{\partial q_{xj}}, \quad A_{ij}^{(2)} = \frac{\partial E_i}{\partial q_{yj}}, \quad A_{ij}^{(3)} = \frac{\partial E_i}{\partial p_j} \tag{3.12}$$

and then join these three matrices to obtain a $3N \times 3N$ result for matrix (A).

Having both E and (A), we use as initial seed $q_x^{(0)} = \{1, \ldots, 1\}$, $q_y^{(0)} = \{0, \ldots, 0\}$ and $p^{(0)} = \{0, \ldots, 0\}$ and join these to form $q^{(0)}$. After this, the method follows automatically as explained in section 2.4.

3.4 Results

Using the method described in the previous section, and after a choice of the parameter λ, we are able to produce results for the velocity and pressure fields of the problem.

Intuitively, we expect the solutions with a high value of λ to be better behaved and less prone to turbulence related instabilities, since in these cases the flow would be slower around the cylinder and the fluid would more easilly circulate the cylinder and meet on the other side at $w = 1$ without causing big turbulent effects. This in turn would make the solution more symmetric in $w = 0$ in the sense that the velocity profile to the left of the cylinder would be much the same as the one to the right, which would not be the case for lower values of λ where, after passing the cylinder, in the area around it, the fluid would become accelerated. For low enough λ turbulent effects would start to dominate the behaviour in this area, causing abrupt changes in the velocity and pressure fields near the cylinder, and a stable stationary solution would be impossible to find due to the very large numerical instabilities they would generate. Finally, a higher λ would also cause the overall velocity

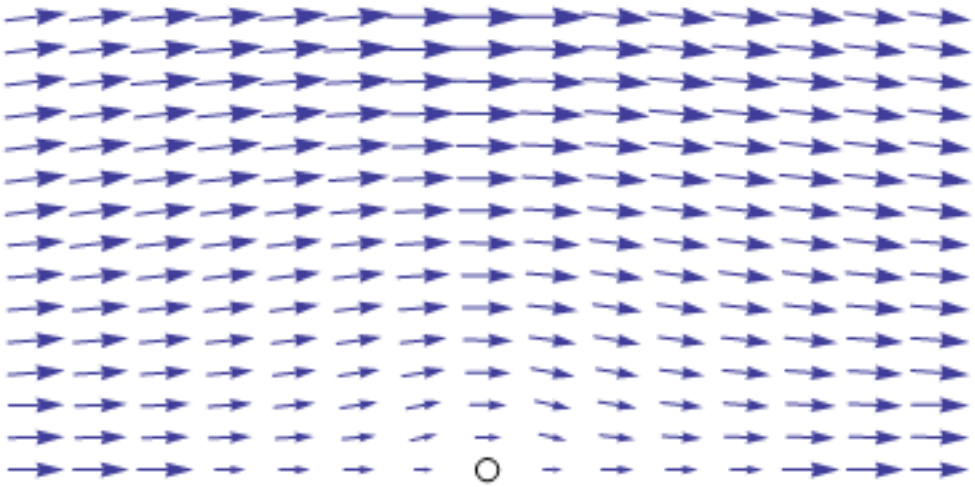

Figure 3.4: Velocity profile of the system with $\lambda = 100$ in Cartesian coordinates.

profile to be affected at a larger distance by the presence of the cylinder, that is, in this case we expect the velocity to go to v_0 at a smaller rate than with lower λ.

Regarding the pressure field, the pressure will obviously be higher in all cases at the region where the flow is approaching the cylinder, and lower where it is flowing away. It should be kept in mind that the actual value for the pressure is irrelevant for our problem, since it does not affect the equations in any way, the gradient is what is important, since it accelerates the fluid from the higher pressure areas to the lower ones. With that in mind, we expect the cases with higher values for λ to have significantly smaller pressure gradients around the cylinder.

We will present solutions for different values of λ and compare them. Starting with a higher value of $\lambda = 100$, we can see how the velocity field behaves in Figure 3.4, where the arrows represent the velocity vector $\vec{u}$ in Cartesian coordinates. The flow is homogeneous until it reaches a certain distance from the cylinder where the effects of its presence start to have the effect of deviating the flow with the appearance of an y component to the velocity.

This occurs because, obviously, the fluid has to go around the cylinder, and with high λ,which is basically high viscosity coefficient in comparison

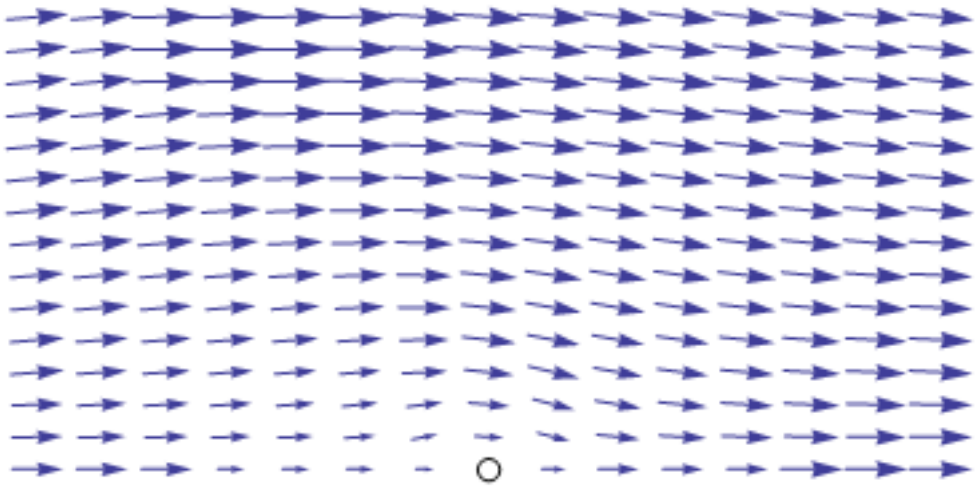

Figure 3.5: Velocity profile of the system with $\lambda = 10$ in Cartesian coordinates.

with the other parameters, the particles of the fluid are more attracted to each other, and a lot of space is needed for the different layers of the fluid to gradually decelerate towards the surface of the cylinder, overcoming the friction between layers required so that they move at different speeds. The velocity field is almost symmetrical in this case, as well as the pressure.

In the case of $\lambda = 10$, presented in Figure 3.5, the radius of influence of the cylinder, i.e., the distance from its surface where it starts to a considerable effect on the behaviour of the fluid, is decreased, since the different layers of the fluid are, in case of smaller viscosity coefficient, less connected, so it accelerates faster to u_∞ in the x direction.

Additionally, despite the fact that the velocity profiles only start undergoing noticeable changes at a smaller radius, these changes are more drastic in this case, with a higher convective acceleration near the cylinder and the appearance of a significant y component to the velocity $\vec{u}$, as we can see in Figure 3.6.

Finally, in the case $\lambda = 1$, the same argument for the decrease of the radius of influence holds, with the effect being obviously more pronounced. In Figure 3.7 we can see that $\vec{u}$ now has a larger y component near the cylinder, and that the apparent symmetry exhibited in the higher λ no longer exists.

The y component of the velocity, plotted in Figure 3.8, can be seen to

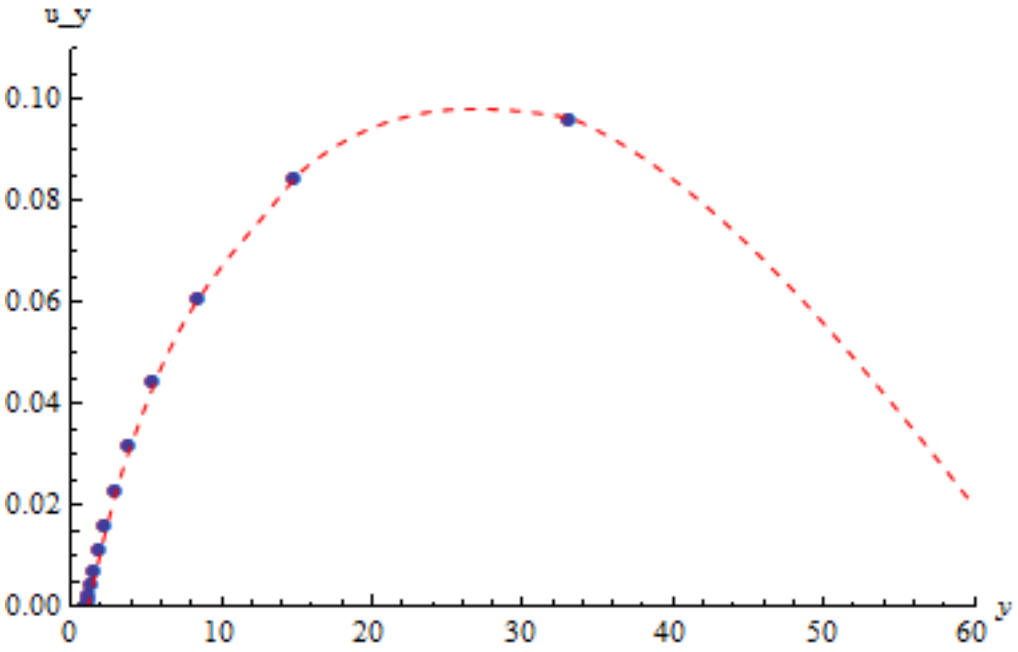

Figure 3.6: y component of the velocity as a function of y in the section $x = 0$ for $\lambda = 10$.

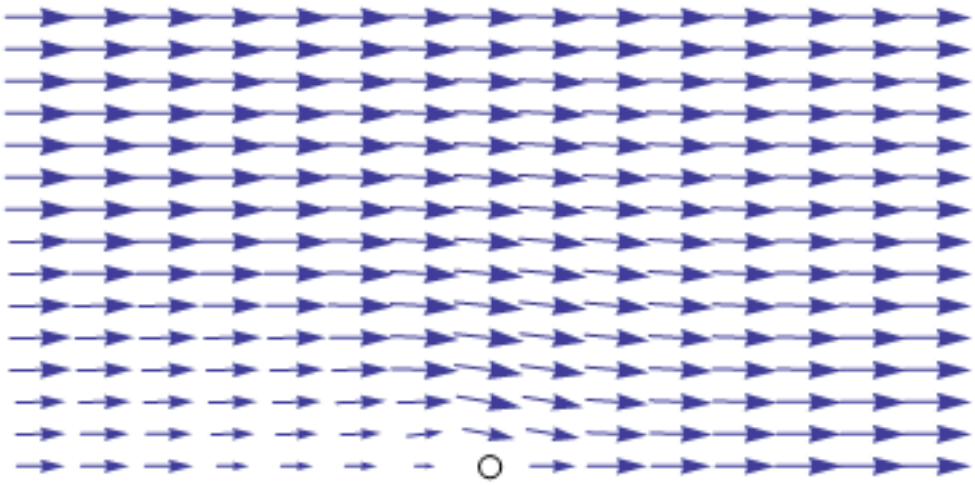

Figure 3.7: Velocity profile of the system with $\lambda = 1$ in Cartesian coordinates.

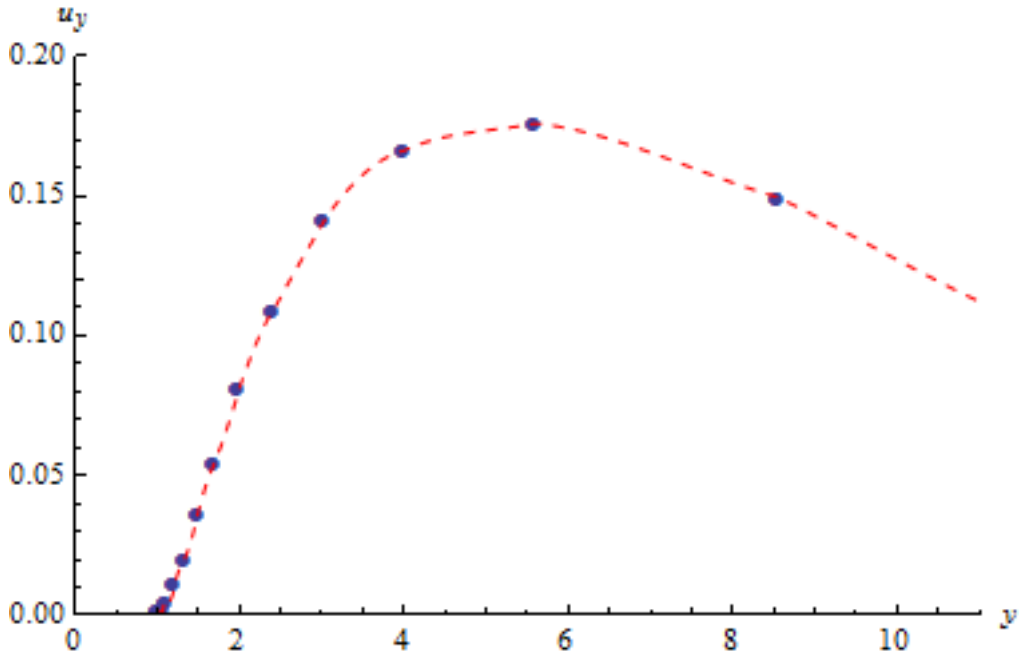

Figure 3.8: y component of the velocity as a function of y in the section $x = 0$ for $\lambda = 1$.

increase to a higher maximum value than in the previous case, but going again to zero at a smaller distance from the cylinder.

For an objective view of the described phenomenon, we plot the x component of the velocity for the three values of λ as a function of the radial coordinate v at $w = \frac{1}{2}$ $(x = 0)$. Figure 3.9 clearly shows that the acceration is larger when λ is smaller, and consequently the distance from the cylinder where its effects are noticeable tends to increase with λ.

To analyze the behaviour of the pressure, we plotted p for different values of λ at the surface of the cylinder in Figure 3.10. It is positive where the flow is approaching the sphere and negative on the other end, so that its gradient accelerates the fluid in the right direction. What is also notorious is the symmetry of the case $\lambda = 100$ being lost when we decrease λ, with the pressure gradient becoming higher as the curve gets steeper in this low viscosity cases.

As a test of the convergence power of the method with the number of points, we compared solutions obtained with grids of different size using a

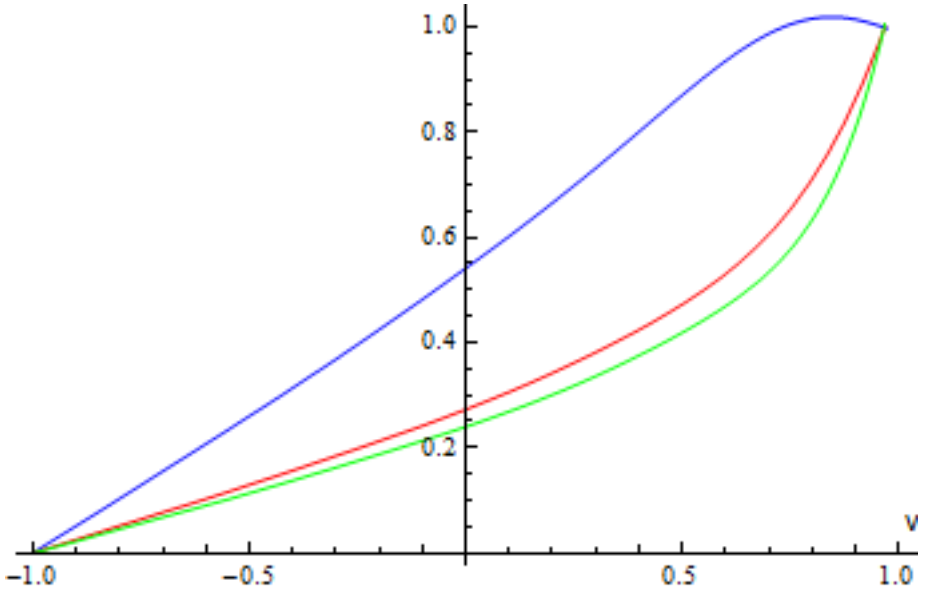

Figure 3.9: x component of the velocity as a function of v in the section $w = \frac{1}{2}$ for $\lambda = 1$ (blue), 10 (red) and 100 (green).

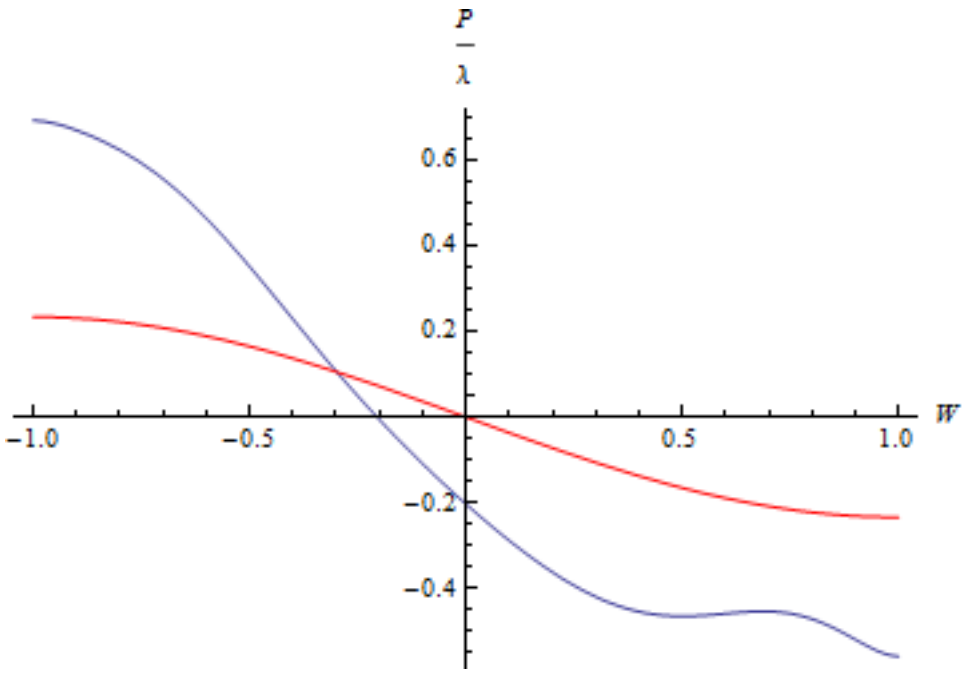

Figure 3.10: Pressure as a function of w at the surface of the cylinder for $\lambda = 10$ (red), and $\lambda = 1$ (blue).

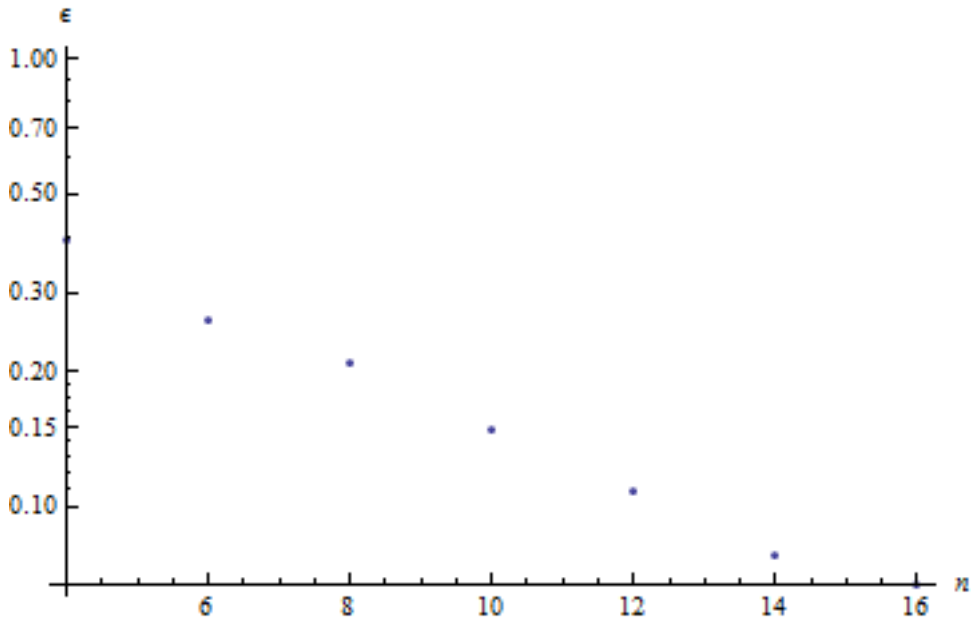

Figure 3.11: Error parameter ϵ as a function of the grid size n.

solution obtained for $n = 20$ as a basis for comparison, and the solutions are converging as we increase the size of the grid. This can be seen in Figure 3.11, where we compare the velocities of solutions obtained with grids of different sizes to the velocity profiles of the solution for $n = 20$, using as a parameter $\epsilon = \sqrt{(v_{xn} - v_{x20})^2 + (v_{yn} - v_{y20})^2}$, whose value decreases approximately exponentially as we increase n.

In conclusion, the parameter λ has the effect of altering the radius on which the effects of the presence of the cylinder are noticed in the behaviour of the velocity and the pressure gradient. As a consequence, it also changes the rate at which these quantities vary. The results obtained are consistent with the physics of the problem and with existent numerical simulations [15] [12].

Chapter 4

Einstein-de Turck method

While simplifying assumptions such as spherical symmetry can enable us to find black hole type solutions of the Einstein-Maxwell equations analytically, like the Schwarzschild or Reissner-Nordstrom solutions, the introduction of external devices to break such a symmetry, such as the polarization of space with an electric field, makes it unlikely that closed form analytic solutions can be found.

The problem of finding these types of black holes then becomes that of solving the non-linear coupled set of partial differential equations given by the Einstein-Maxwell equations, and if we want to understand the properties of said objects we must turn to numerical techniques to tackle these PDEs. So the first question we ask about these PDEs is what character they have, since this will determine how to approach the problem.

If we wanted to consider dynamics we would want the equations to display an hyperbolic character, which would allow us to think of the equations as an initial value problem, with data being specified on a past light cone and on small scales having wave-like propagation.

However, we are interested in finding static and stationary black holes, so the problem should be thought of as having elliptic character, since one solves elliptic systems as boundary value problems where one piece of data (for example Dirichlet, Newmann, Robin, ...) is given on all boundaries. Physically, such boundary conditions in our case will correspond to ensuring

horizon regularity and prescribing an asymptotic behaviour, as discussed on the next chapter.

4.1 Elliptic boundary value problems

A second order differential equation

$$Au_{xx} + 2Bu_{xy} + Cu_{yy} + Du_x + Eu_y + F = 0 \tag{4.1}$$

is termed elliptic if the matrix

$$Z = \begin{bmatrix} A & B \\ B & C \end{bmatrix} \tag{4.2}$$

is positive definite. As with a general PDE, elliptic PDE may have non-constant coefficients and be non-linear. Despite this variety, the elliptic equations have a well-developed theory.

Examples of elliptic PDE are the Laplace equation $\nabla^2 u = 0$ or the non-homogenous Poisson equation $\nabla^2 u = f(x)$. Boundary conditions are used in problems involving elliptic PDEs, to give constraints $u(x, y) = g(x, y)$ on $\partial\Omega$. An elliptic boundary value problem can then be thought of as the stable state of an evolution problem. Using our previous example, the Laplacian with Dirichlet boundary conditions gives the eventual distribution of heat in a room several time after the heating is turned on, when the system has reached a stationary state, but the problem itself does not involve the time variable, instead only depending on space variables. This is precisely the situation we want to adress in our problem, ignoring its dynamics, we want to get information about the stable state (if there is any).

In an operator equation, the principal part of a differential operator is composed by the higher order terms of its symbol, it is the only part of its symbol that transforms as a tensor under changes to the coordinate system, and it controls almost completely the qualitative behaviour of solutions to a PDE, in particular elliptic partial differential equations can be characterized by those whose principal symbol is nowhere zero.

4.2 Harmonic Einstein equation

First, we want to ensure the horizon has a smooth geometry, so that we are free to choose our coordinates to impose a boundary there. This can be done by analytic continuation of the time coordinate of the static black hole.

If we consider a general non-extremal static black hole solution with a single component horizon we may write the metric as [31]

$$ds^2 = -N^2(x)dt^2 + h_{ij}(x)dx^i dx^j \tag{4.3}$$

Any such black hole can be analytically continued to imaginary time $\tau = i\ t$ to yield a Riemannian manifold with metric

$$ds^2 = N^2(x)d\tau^2 + h_{ij}(x)dx^i dx^j \tag{4.4}$$

This Euclidean continuation introduces an angular coordinate τ with period $\frac{2\pi}{\kappa}$ where κ is the surface gravity of the black hole. The proper size of this Euclidean time circle has the interpretation of being the inverse of the temperature of the black hole. So, far from the black hole, we can impose boundary conditions on the metric that involve fixing (among other things) its temperature. Changing these boundary conditions later will provide a simple way to flow from one solution to others.

Solving the vacuum Einstein equation is equivalent to finding a geometry that is Ricci flat, so $R_{\mu\nu} = 0$. With the metric above this can be seen as part of the more general problem of finding Ricci flat Riemannian geometries.

The vacuum Einstein equation $R_{\mu\nu} = 0$ is a second order non-linear PDE in the metric. If we perturb the metric about some background $g_{\mu\nu}$ by a perturbation $h_{\mu\nu}$, then the change to the Ricci tensor is given by

$$\delta R_{\mu\nu} \equiv \Delta_R h_{\mu\nu} = \Delta_L h_{\mu\nu} + \nabla_{(\mu} v_{\nu)} \tag{4.5}$$

where

$$\begin{aligned} \Delta_L h_{\mu\nu} &= -\frac{1}{2}\nabla^2 h_{\mu\nu} - R_{\mu\ \nu}^{\ \kappa\ \lambda} h_{\kappa\lambda} + R_{(\mu}^{\ \ \kappa} h_{\nu)\kappa} \\ v_\mu &= \nabla_\nu h^\nu_{\ \mu} - \frac{1}{2}\partial_\mu h \end{aligned} \tag{4.6}$$

where Δ_L is the Lichnerowicz Laplacian.

The principal part of Δ_R, which we denote P_g, is given by only taking the higher order, two derivative terms

$$P_g h_{\mu\nu} = \frac{1}{2} g^{\alpha\beta} \left(\partial_\mu \partial_\alpha h_{\beta\nu} + \partial_\nu \partial_\alpha h_{\beta\mu} - \partial_\alpha \partial_\beta h_{\mu\nu} - \partial_\mu \partial_\nu h_{\alpha\beta} \right) \tag{4.7}$$

and it controls the short wavelength behaviour of perturbations, which in turn determines the character of the equations $R_{\mu\nu}$ about the background g.

The condition that $R_{\mu\nu} = 0$ being elliptic gives the requirement that if we take $h_{\mu\nu} = a_{\mu\nu} e^{i k_\alpha x^\alpha}$ for some constants $a_{\mu\nu}$ and any vector k_μ, then $P_g h_{\mu\nu} = 0$ if and only if $k = 0$, which means that there are no points where short wavelength perturbations propagate as a wave. This is not generally the case with 4.7.

We can always change the coordinate system we are working with, changing the metric $h_{\mu\nu} \to h_{\mu\nu} + \nabla_{(\mu} \Lambda_{\nu)}$. Obviously, this does not change any phyisical properties of the system, so we can just change our equations by fixing a coordinate system, and instead of considering $R_{\mu\nu} = 0$ we will consider what we term the harmonic Einstein equation [31], $R^H_{\mu\nu} = 0$, where

$$\begin{aligned} R^H_{\mu\nu} &= R_{\mu\nu} - \nabla_{(\mu} \xi_{\nu)} \\ \xi^\alpha &= g^{\mu\nu} \left(\Gamma^\alpha{}_{\mu\nu} - \bar{\Gamma}^\alpha{}_{\mu\nu} \right) \end{aligned} \tag{4.8}$$

Γ is the Levi-Civita connection for the metric g, and $\bar{\Gamma}$ is another connection for a reference metric we are free to choose, and then consider fixed, termed reference connection. The De Turck vector ξ is then constructed from the difference of two connections, so it is a globally defined vector field.

The metric we term reference metric can be any metric we choose (even the simple Schwarzchild black hole), and we will show that, with the use of this method, it can lead to other, more complicated solutions (like Reissner-Nordstrom). Obviously, the closer the reference metric is to the metric we are searching for, the faster we will reach that solution, with less computational costs.

The principal part of Equation 4.8 is now simply given by

$$P_g^H h_{\mu\nu} = -\frac{1}{2} g^{\alpha\beta} \partial_\alpha \partial_\beta h_{\mu\nu} \tag{4.9}$$

If we now take $h_{\mu\nu} = a_{\mu\nu} e^{ik_\alpha x^\alpha}$, then $P_g^H h_{\mu\nu} = a_{\mu\nu} k^\alpha k_\alpha$, which is indeed nonzero everywhere for any real non-zero k_μ (using our metric with Euclidean signature).

The condition $\xi^\mu = 0$ provides D local conditions, thereby eliminating any local coordinate degrees of freedom from the problem [23]. This, however, will require extra attention when analyzing possible solutions to the harmonic Einstein equation, since this choice of gauge fixes the coordinate system on which these solutions will be obtained.

4.3 Ricci flat solutions vs. Ricci solitons

While a Ricci flat solution with $\xi = 0$ does indeed solve the Harmonic Einstein equation, there is in principle no guarantee that a solution to this equation is also a solution to the Ricci flatness condition. It would seem that solving $R_{\mu\nu}^H = 0$ is therefore a totally different problem as that of solving $R_{\mu\nu} = 0$.

A solution to $R_{\mu\nu}^H = \nabla_{(\mu}\xi_{\nu)}$ with non vanishing ξ is called a Ricci soliton. We are not interested in these types of solutions, but rather in Ricci flat solutions. So, the problem becomes that of, once we obtain a solution for the Harmonic Einstein equation, distinguishing between both these types.

Fortunately, the existence of Ricci solitons is highly constrained provided we choose our boundary conditions appropriately. It can be proven for certain solutions of interest that, despite the fact that we are solving the Harmonic Einstein equation, the only solutions are in fact Ricci flat solutions with the gauge condition $\xi^\mu = 0$ imposed [31].

The details of this are not important because, even if solitons do exist, this is not necessarily a problem, since to identify one of those types of solutions we can simply compute for example the vector field ξ and see if it is zero, or the scalar norm of ξ, $\phi = \xi^\mu \xi_\mu$. For a Riemannian manifold $\xi = 0$ is a necessary condition for ϕ to vanish. Therefore, checking the magnitude of ϕ

is a good way to distinguish between solitons and Ricci flat solutions. Since the equations we are using are elliptic, for well posed boundary conditions on the metric we expect the solutions to be locally unique, and as a consequence a solution cannot be continuously deformed into another without adjusting the boundary conditions, so if we run into a solution that is a soliton, we can recognize it and adjust our problem so as to try to find another one.

Chapter 5

Black Holes in AdS space

We will now turn our attention to, using the methods described so far, finding black hole type solutions to the Einstein-Maxwell equations in a space with a negative cosmological constant (anti de Sitter space). We will introduce the action from which the equations arise and the general form of the metric, along with suitable boundary conditions for the problem.

5.1 Einstein-Maxwell-Λ equations

We start by taking the Einstein-Maxwell-Λ action in four dimensions, given by

$$S = \int d^4x\sqrt{-g}\left(R - 2\Lambda - \frac{1}{4}F^2\right), \tag{5.1}$$

where Λ is the cosmological constant, R is the Ricci tensor, and F is the electromagnetic field tensor $F = \mathrm{d}A$ (A is the electromagnetic potential), and then use the variational principle $\delta S = 0$ to obtain the equations of motion. We can separate 5.1 into a gravitational part

$$S_g = \frac{1}{16\pi}\int d^4x\sqrt{-g}\left(R + \frac{6}{L^2}\right)$$

where we write $\Lambda = -\frac{3}{L^2}$, and an electromagnetic part

$$S_{em} = -\int d^4x\sqrt{-g}\left(\frac{1}{4}F^2\right).$$

Using $\delta\sqrt{-g} = \frac{1}{2}\sqrt{-g}g^{\alpha\beta}\delta g_{\alpha\beta}$ and $\delta g^{\alpha\beta} = -g^{\alpha\mu}g^{\beta\mu}\delta g_{\mu\nu}$, we arrive at the following equations of motion

$$G_{\alpha\beta} - \Lambda g_{\alpha\beta} = 2T_{\alpha\beta} \tag{5.2}$$

where G is the Einstein tensor defined as $G_{\alpha\beta} = R_{\alpha\beta} - \frac{1}{2}R$, and

$$T_{\alpha\beta} = \frac{2}{\sqrt{-g}}\frac{\delta S_{em}}{\delta g_{\alpha\beta}} = F_{\alpha\mu}F_{\beta}{}^{\mu} - \frac{1}{4}g_{\alpha\beta}F^2. \tag{5.3}$$

Taking the trace of 5.2, we can write Λ in terms of the Ricci scalar

$$R - 2R + 4\Lambda = 0 \implies \Lambda = \frac{R}{4} \tag{5.4}$$

and equation 5.2 becomes

$$R_{\mu\nu} - \frac{R}{4}g_{\mu\nu} = 2T_{\mu\nu}, \tag{5.5}$$

while the Maxwell equation is given by

$$\nabla^{\mu}F_{\mu\nu} = 0. \tag{5.6}$$

5.2 Exact Solutions

Equations 5.5 are equations for the metric components $g_{\mu\nu}$, to which exact solutions exist, and the AdS space is such an exact solution with a negative cosmological constant. It is given by the metric [33]

$$ds^2 = -\left(1 + \frac{r^2}{L^2}\right)dt^2 + \frac{dr^2}{\left(1 + \frac{r^2}{L^2}\right)} + r^2 d\Omega_2^2 \tag{5.7}$$

where $d\Omega_2^2$ is the metric for a 2-sphere

$$d\Omega_2^2 = d\theta^2 + \sin^2\theta d\phi^2 \tag{5.8}$$

and L is the radius of curvature of spacetime.

One of the important features of the AdS spacetime that motivated its study was that it behaves much like a box - it has an infinite potential wall at asymptotic infinity. To see this, let us consider a particle with four momentum $P^\mu = (E, p^1, p^2, p^3)$. An observer at infinity has four velocity $U^\mu = \frac{k^\mu}{\sqrt{-k^2}}$, where $k = \frac{\partial}{\partial t}$. The energy measured by the local observer is

$$E_O = -g_{\mu\nu} U^\mu P^\nu = \frac{E}{\sqrt{-k^2}} = \frac{E}{\sqrt{-g_{tt}}}$$

and since, according to 5.7, $-g_{tt} = 1 + \frac{r^2}{L^2}$, E is red shifted to 0 at $r \to \infty$. This reflects the fact that AdS space has an infinite potential wall at asymptotic infinity.

The only static and spherically symmetric black hole type solution in AdS space to

$$R_{\mu\nu} - \frac{R}{4} g_{\mu\nu} = 0 \tag{5.9}$$

is given by the Schwarzschild-AdS metric [33]

$$ds^2 = -f(r) dt^2 + \frac{dr^2}{f(r)} + r^2 d\Omega_2^2 \tag{5.10}$$

where $f(r)$ is the function

$$f(r) = 1 - \frac{2M}{r} + \frac{r^2}{L^2} \tag{5.11}$$

where M is the mass of the black hole.

This metric can be seen to be singular at $r = 0$ (curvature singularity $R_{abcd} R^{abcd} \approx r^{-6}$) and $r = r_0$ (coordinate singularity), where r_0 is the horizon radius of the black hole. To determine a relation between this radius and the other parameters of the problem, we need to solve $f(r_0) = 0$, yielding

$$M = \frac{r_0 (L^2 + r_0^2)}{2L^2} \tag{5.12}$$

When we add a global charge to the problem, equation 5.6 admits as a

solution an electromagnetic potential given by

$$A = \left(\frac{Q}{r} - \frac{Q}{r_0}\right) dt \tag{5.13}$$

where Q is the charge of the black hole, so we need an exact solution to equation 5.4 with the field strength tensor obtained by this potential.

That solution is the Reissner-Nordstrom-AdS metric, given by 5.10, where $f(r)$ is the function

$$f(r) = 1 - \frac{2M}{r} + \frac{r^2}{L^2} + \frac{Q^2}{r^2} \tag{5.14}$$

The condition $f(r_0) = 0$ in this case yields the relation

$$M = \frac{r_0^4 + L^2(Q^2 + r_0^2)}{2r_0 L^2} \tag{5.15}$$

5.2.1 Thermodynamics

One way to find the temperature of a black hole is by calculating its surface gravity, but a more direct way is to do an analytic continuation of the metric 5.10 to Euclidean time, by performin a Wick rotation $t = i\tau$,

$$ds^2 = f(r)d\tau^2 + \frac{dr^2}{f(r)} + r^2 d\Omega_2^2 \tag{5.16}$$

and then expanding the metric near the horizon $r = r_0$, by setting

$$f(r) = (r - r_0)f'(r_0) + O(r - r_0)^2 \tag{5.17}$$

and inserting this on the metric 5.16

$$ds^2 = (r - r_0)f'(r_0)d\tau^2 + \frac{dr^2}{(r - r_0)f'(r_0)} + r_0^2 d\Omega_2^2 \tag{5.18}$$

Making the substitution $r = r_0 + \frac{1}{4}f'(r_0)q^2$, then $dr = \frac{1}{2}f'qdq$ and

$$ds^2 = dq^2 + \left(\frac{f'(r_0)}{2}\right)^2 q^2 d\tau^2 + r_0^2 d\Omega_2^2 \tag{5.19}$$

Note that the first two terms of 5.19 resemble the polar coordinates $ds^2 = dr^2 + r^2 d\theta^2$. If this θ has period 2π, then it is the metric of the flat plane, while different periodicities would result in a conical singularity at $r = r_0$. To avoid such defects, τ needs to be periodic with period $\beta = 2\pi \frac{2}{f'(r_0)}$. It is a well known fact [33] [10] that the temperature of a black hole is the inverse of this period, which yields the temperature as

$$T = \beta^{-1} = \frac{1}{2\pi} \frac{f'(r_0)}{2} \tag{5.20}$$

For the case of Schwarzschild-AdS

$$f'(r_0) = \frac{L^2 + 3r_0^2}{r_0 L^2} \tag{5.21}$$

so the temperature is given by

$$T(r_0) = \frac{L^2 + 3r_0^2}{4\pi r_0 L^2} \tag{5.22}$$

If we plot the temperature against the horizon radius of the black hole (Figure 5.1), we see that unlike the asymptotically flat case, the Schwarzschild-AdS black hole temperature no longer decreases monotonically with r_0. It attains a minimum T_0 at $r_{min} = \frac{L}{\sqrt{3}}$ and then increases without bound.

For $T < T(r_{min})$, black holes cannot exist and the space is filled with pure radiation. At any $T > T(r_{min})$, there are two possible black hole solutions. The smaller black hole, represented by the branch with $r_0 < r_{min}$, has negative specific heat and is thermodynamically unstable. The larger black hole, represented by the branch with $r_0 > r_{min}$, has positive specific heat and is thermodynamically stable, and will be the one we want to study.

In the case of a charged black hole, the temperature is given by

$$T(r_0) = \frac{L^2(r_0^2 - Q^2) + 3r_0^4}{4\pi r_0^3 L^2} \tag{5.23}$$

and plotting it against the horizon radius we see that the changes to the asymptotically flat case are similar, it no longer decreases with r_0, and al-

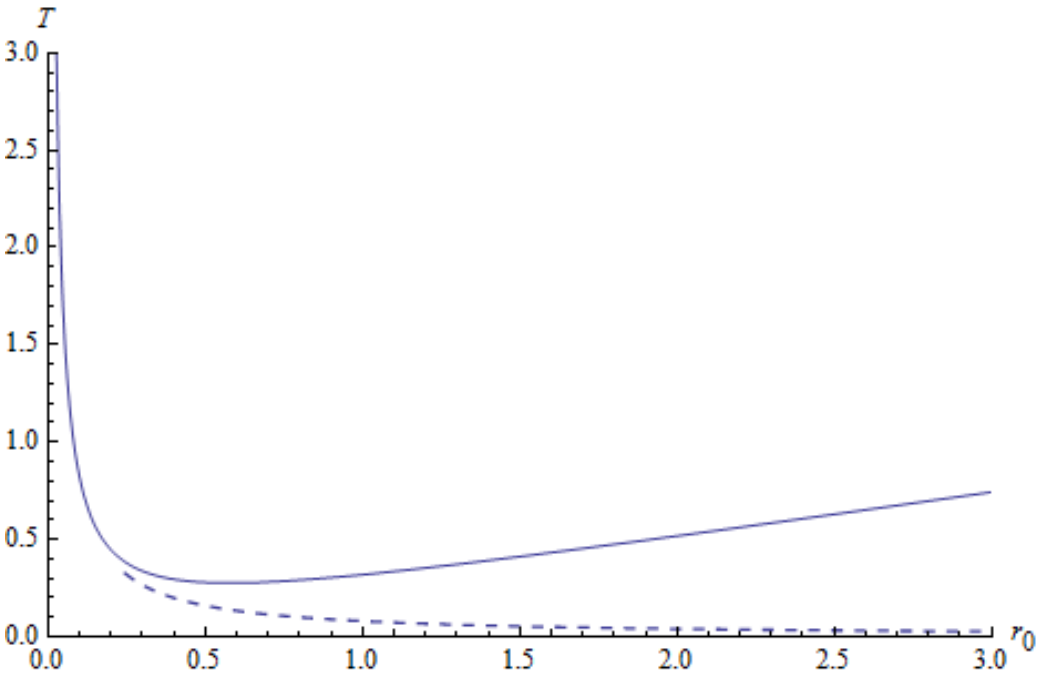

Figure 5.1: Temperature as a function of r_0 for a Schwarzschild black hole in flat (dashed) and AdS $L = 1$ (solid) space.

though there is now in principle no minimum T_0, there is an r_{0min}, and the size of the horizon grows boundlessly with the temperature.

Another thermodynamical quantity of interest for the study of black holes is entropy, which is given by [22]

$$S_{BH} = \frac{A}{4}$$

where A is the surface area of the black hole horizon. For a spherically symmetric black hole, this is just $A = 4\pi r_0^2$, so the entropy grows with the horizon radius, and consequently with the temperature, for the case of black holes in AdS space.

Hawking-Page phase transition

An even more interesting thermodynamical feature of the Schwarzschild-AdS solution is that it exhibits a first order phase transition. In order to discuss this, we will first introduce some quantum field theory formalism which is

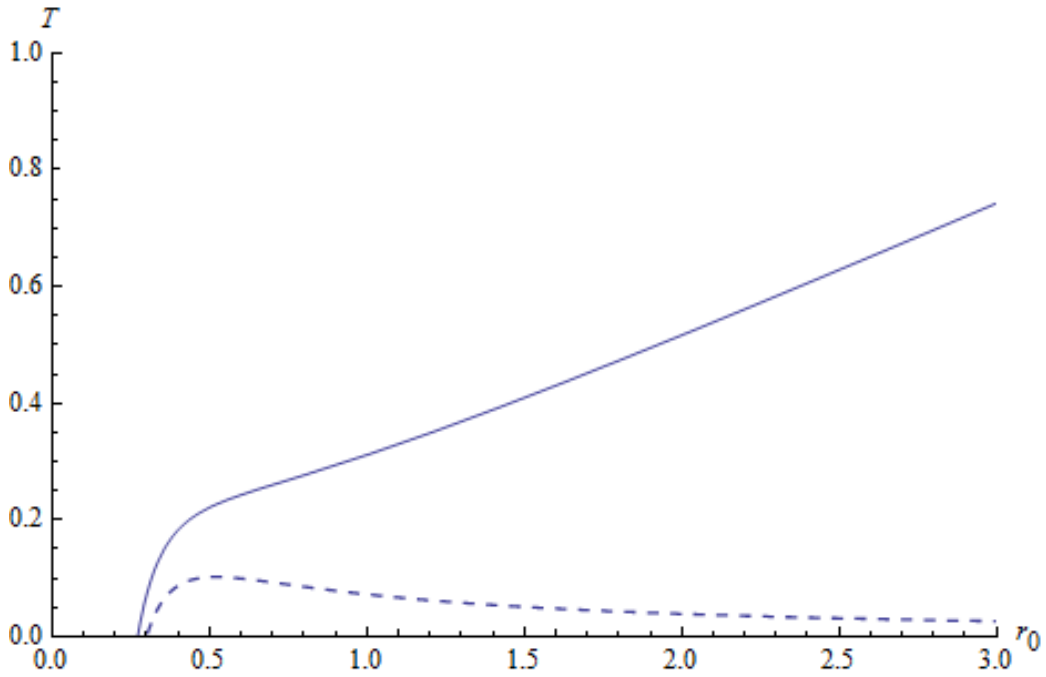

Figure 5.2: Temperature as a function of r_0 for a Reissner-Nordstrom $Q = 0.3$ black hole in flat (dashed) and AdS $L = 1$ (solid) space.

used to define a partition function that can be used to derive several thermodynamic variables.

In quantum field theory, the amplitude for a field with a configuration ϕ_1 to propagate to a configuration ϕ_2 can be written as [33]

$$Z =< \phi_2 | e^{-iH(t_2 - t_1)} | \phi_1 >$$

If we perform an analytical continuation to Euclidean time $\tau = it$, and set the initial and final field configurations $\phi_1 = \phi_2 = \phi$, then $\tau_2 - \tau_1 = \beta$ is just the period in which the field goes back to its original configuration. If we integrate over all ϕ then

$$Z = \mathrm{Tr} e^{-\beta H} \tag{5.24}$$

where now the integral is taken over all fields that are periodic in imaginary time with period β. This is simply the partition function of ϕ at temperature $T = \beta^{-1}$. Hence we are justified in identifying the inverse period of the imaginary time with the temperature of the solution.

The partition function plays a central role in statistical mechanics because many thermodynamic quantities of interest can be derived from it. For example, the expectation value for the energy and the entropy are given by [22]

$$< E >= -\frac{\partial}{\partial\beta} Z, \qquad S = \beta < E > + \log Z \tag{5.25}$$

Using the path integral formalism, the partition function is given by $Z = \int D\phi e^{-I[\phi]}$, where we have already continued to imaginary time to make the integral convergent and are using I for the action. The dominant contribution to the path integral comes from the minima of the action where $\delta I = 0$, thus we can approximate the path integral by $Z \approx e^{-I}$ or $\log Z = -I$. It is useful to define the free energy $F = -T \log Z = TI$, so that, when we are faced with multiple minima, the one with the lowest free energy will be favoured because it dominates the partition function. When we are dealing with curved spacetimes, the path integral must be generalized to account for variations of the field ϕ as well as the metric g, so we can write it as $Z = \int D[g, \phi] e^{-I[g,\phi]}$.

The action for Schwarzschild-Ads is given by

$$I = \frac{1}{16\pi} \int_M d^4x \sqrt{g}(R - 2\Lambda) + S_{GHY} \tag{5.26}$$

where S_{GHY} is the Gibbons-Hawking-York boundary term, a term that needs to be added to the Einstein-Hilbert action for the path integral approach[17]. As an example, consider flat space where $R = 0$. In this case this term completely determines the action of the system, and consequently its partition function and all its thermodynamical properties. In AdS, however, it will not contribute to the computation we want to perform, since it cancels out while taking the difference between the actions of AdS space and of a Schwarzschild-AdS black hole. It is given by

$$S_{GHY} = \frac{1}{8\pi} \int_{\partial M} d^3x \sqrt{h} K \tag{5.27}$$

where h is the induced metric on the boundary and K is the trace of the

second fundamental form $K_{\mu\nu}$, given by

$$K_{\mu\nu} = \frac{1}{2} n_\alpha h^{\alpha\beta} \partial_\beta h_{\mu\nu} \tag{5.28}$$

where the n is the unit vector normal to the surface, $n_\alpha = \frac{\delta_\alpha^r}{\sqrt{g_{rr}}}$. The trace is then

$$K = \frac{1}{\sqrt{f(r)}} \left(\frac{M}{r^2} + \frac{r}{L^2} \right) + \sqrt{f(r)} \frac{2}{r} \tag{5.29}$$

and, for the case of Schwarzschild-AdS (we regularize the infinite integral by integrating the radial variable up to a cutoff radius R)

$$S_{GHY}^{(BH)} = \frac{\Lambda}{2} \beta \left(2R - 3M + \frac{3R^2}{L^2} \right) \tag{5.30}$$

For the case of pure AdS, we just have to set $M \to 0$, so

$$S_{GHY}^{(AdS)} = \frac{\Lambda}{2} \beta_1 \left(2R + \frac{3R^2}{L^2} \right) \tag{5.31}$$

where β_1 can be obtained by equating the proper length of the time circles at $r = R$

$$\frac{\beta_1}{\beta} = \sqrt{1 - \frac{2M}{R + \frac{R^3}{L^2}}} \tag{5.32}$$

Now we can compute the difference between these terms

$$S_{GHY}^{(BH)} - S_{GHY}^{(AdS)} = \frac{\Lambda}{2} \beta \left(-3M + \frac{M}{1 + \frac{R^2}{L^2}} (2 + 3\frac{R^2}{L^2}) \right) \tag{5.33}$$

and, for large R,

$$S_{GHY}^{(BH)} - S_{GHY}^{(AdS)} = \frac{\Lambda}{2} \beta \left(-3M + 3\frac{ML^2}{R^2} \frac{R^2}{L^2]} \right) = 0 \tag{5.34}$$

Since the surface terms do not contribute, and as we have shown in 5.5, $R = 4\Lambda$, the action reduces to the volume integral

$$I = \frac{\Lambda}{8\pi} \int d^4x \sqrt{g} \tag{5.35}$$

which is infinite if we integrate over all space. Again, we need to regularize it by integrating the radial variable only up to some cutoff value $r = K$. For the AdS space (without black hole)

$$I_{Ads} = \frac{\Lambda}{8\pi}\int_0^{\beta_1} dt \int_0^K r^2 dr \int_{S^2} d\Omega_2^2 = \frac{\Lambda}{6}\beta_1 K^3 \tag{5.36}$$

while for the Schwarzschild-AdS case,

$$I_{BH} = \frac{\Lambda}{8\pi}\int_0^{\beta_0} dt \int_{r_0}^K r^2 dr \int_{S^2} d\Omega_2^2 = \frac{\Lambda}{6}\beta_0 (K^3 - r_0^2) \tag{5.37}$$

While β_0 is given by 5.22, β_1 can in principle take any value, since there is no requirement that the AdS metric is periodic in time. One must adjust β so that the geometry of the hypersurface $r = K$ is the same in the two cases, since the Schwarzschild AdS metric, far enough from the black hole horizon, asymptotes to AdS. This requires that the proper length of the time circles at $r = K$ precisely match, so

$$\beta_1\sqrt{1 + \frac{K^2}{L^2}} = \beta_0\sqrt{1 + \frac{K^2}{L^2} - \frac{2M}{K}} \tag{5.38}$$

Thus the difference between Euclidean actions is

$$I = I_{BH} - I_{AdS} = \frac{\Lambda}{6}\beta_0\left((K^3 - r_0^3) - \frac{\beta_1}{\beta_0}K^3\right) = -\frac{\beta_0}{2L^2}\left(K^3 - r_0^3 - K^3\sqrt{1 - \frac{2ML^2}{L^2K + K^3}}\right) \tag{5.39}$$

and, for large K,

$$I \approx \frac{\beta_0}{2L^2}(r_0^3 - ML^2) = \frac{\pi r_0^2(L^2 - r_0^2)}{L^2 + 3r_0^2} \tag{5.40}$$

where we have used 5.12 for M. Using 5.25 we can compute the expected energy and entropy

$$< E >= \frac{\partial I}{\partial \beta_0} = M, \qquad S = \beta_0 < E > -I = \pi r_0^2 \tag{5.41}$$

as is expected for a black hole of mass M and horizon radius r_0.

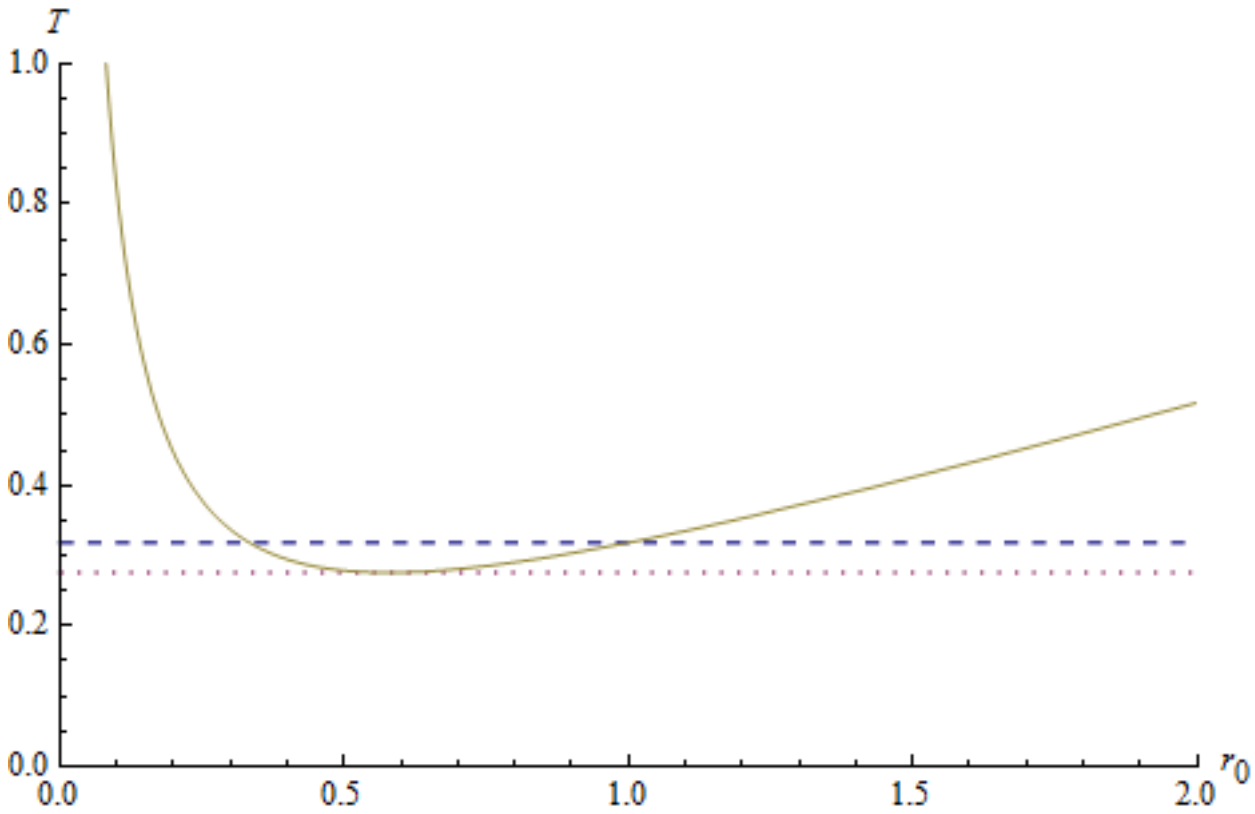

Figure 5.3: Temperature of a Schwarzschild-AdS black hole as a function of r_0 (solid line); T_0 (dotted) and T_c(dashed).

At $r_0 = L$, $I = 0$ and $T_c = (\pi L)^{-1}$, which corresponds to the temperature of a phase transition, in which the preferred state switches from AdS to large black holes, and this is called the Hawking-Page phase transition [22]. As we saw previously, there is another temperature T_0 which is the minimum temperature for a black hole to be able to form (Figure 5.3). The difference between the two temperatures T_0 and T_c indicates the existence of a region of temperatures $T_0 < T < T_c$ in which the preferred state is a radiation gas in AdS, but where black holes are able to form and be in metastable equilibrium with the radiation background. For $T > T_c$, the preferred state will always be a black hole state, but there will also be a temperature which we name T_2 for which radiation must collapse and the universe must have a black hole [33]. A brief summary of this is presented in Figure 5.4.

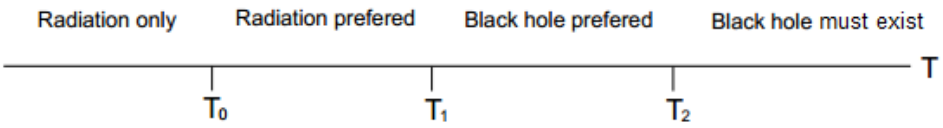

Figure 5.4: Phase diagram for the Hawking-Page phase transition (not to scale).

The Gibbs free energy is given by $F = TI$, so, using 5.22 and 5.40,

$$F = \frac{r_0(L^2 - r_0^2)}{4L^2} \tag{5.42}$$

and this allows us to confirm that the larger ($r_0 > L$) black holes are thermodinamically preferred to the smaller ones of the same temperature.

5.3 Einstein-de Turck equation

As we mentioned in the previous chapter, it is not exactly 5.4 we want to solve, since it is not an eliptic equation, which we need it to be to have a well posed boundary value problem. In order to make the problem elliptic, we make the substitution

$$R_{\mu\nu} \to R_{\mu\nu} - \nabla_{(\mu}\xi_{\nu)} \tag{5.43}$$

where ξ is the de Turck vector defined in 4.8. So, the equations we want to discretize with the use of spectral methods are given by

$$\begin{aligned} R_{\mu\nu} - \nabla_{(\mu}\xi_{\nu)} + \frac{3}{L^2}g_{\mu\nu} - 2T_{\mu\nu} &= 0 \\ \nabla^{\mu}F_{\mu\nu} &= 0 \end{aligned} \tag{5.44}$$

We must also introduce a new set of coordinates adequate to the discretization of the problem on a grid. We take

$$\rho^2 = 1 - \frac{r_0}{r}; \qquad \sin(\theta) = 4x(1-x) \tag{5.45}$$

which have domain $\rho, x \in [0, 1]$. The RN (or Schwarzschild, if we set $Q = 0$)

metric in these coordinates is then

$$\begin{aligned} ds^2 &= \frac{\rho^2}{(1-\rho^2)^2}\tilde{f}(\rho)dt^2 + \frac{4r_0^2}{(1-\rho^2)^2\tilde{f}(\rho)}d\rho^2 + \frac{r_0^2}{(1-\rho^2)^2}d\Omega_2^2 \\ d\Omega_2^2 &= \frac{16}{(1+4x-4x^2)}dx^2 + 16(1-x)^2x^2d\phi^2 \end{aligned} \tag{5.46}$$

where

$$\tilde{f}(\rho) = 1 + 3r_0^2 + (1+r_0^2)\rho^4 - (2+3r_0^2)\rho^2 - Q^2\frac{(1-\rho^2)^3}{r_0^2} \tag{5.47}$$

and we have taken the AdS radius $L = 1$ (resulting in $\Lambda = -3$), as will be done for the rest of this work.

Metric 5.46 will be our reference metric, where we will set r_0 and Q to values that we think are close to the ones we are looking for in our solution. That solution will be another metric, and as an ansatz we take

$$\begin{aligned} ds^2 = \tilde{f}(\rho)\frac{F_1(\rho,x)\rho^2}{(1-\rho^2)^2}dt^2 + \frac{F_2(\rho,x)}{\tilde{f}(\rho)}\left(\frac{2r_0}{1-\rho^2}d\rho + F_3(\rho,x)dx\right)^2 + \\ + \frac{r_0^2}{(1-\rho^2)^2}\left(\frac{16F_4(\rho,x)}{1+4x-4x^2}dx^2 + 16(1-x)^2x^2F_5(\rho,x)d\phi^2\right) \end{aligned} \tag{5.48}$$

along with

$$A = F_6(\rho,x)\frac{\rho^2}{r_0}dt \tag{5.49}$$

and we want to find solutions for the functions $F_i,\ i \in \{1,...,6\}$ for various situations of interest. Since we have introduced an off-diagonal term in the metric, there will be 6 independent equations from equations 5.44, five from the Einstein tensor equation and one from the covariant Maxwell equation. Note that we have constructed our ansatz in such a way that it gives ourselves the freedom to break spherical symmetry, as will be required when we are dealing with polarized black holes.

5.4 Boundary conditions

We will now introduce suitable boundary conditions for the functions F_i.

5.4.1 Horizon and asymptotic behaviour

To study the boundary conditions for this problem, we want to check the behaviour of the system near the boundaries. Considering the expansions of the functions present in equation 5.48, where we first want to expand around the horizon $\rho = 0$

$$\begin{aligned} F_1(\rho, x) &= \sum_0^{n_{max}} a_n(x)\rho^n \\ F_2(\rho, x) &= \sum_0^{n_{max}} b_n(x)\rho^n \\ F_3(\rho, x) &= \sum_0^{n_{max}} e_n(x)\rho^n \\ F_4(\rho, x) &= \sum_0^{n_{max}} c_n(x)\rho^n \\ F_5(\rho, x) &= \sum_0^{n_{max}} f_n(x)\rho^n \\ F_6(\rho, x) &= \sum_0^{n_{max}} d_n(x)\rho^n \end{aligned} \tag{5.50}$$

Substituting into the equations, the conditions for the coefficients obtained will be the boundary conditions

$$\begin{aligned} a_0 &= b_0 \\ e_0 &= 0 \\ a_1 &= 0 \\ b_1 &= 0 \\ c_1 &= 0 \\ d_1 &= 0 \\ f_1 &= 0 \\ &\dots \end{aligned} \tag{5.51}$$

which basically say that the functions F_i $(i = 1, 2, 4, 5, 6)$ cannot be functions of ρ, but of ρ^2, or

$$\frac{\partial f_i}{\partial \rho}|_{\rho=0} = 0 \tag{5.52}$$

Expanding around $\rho = 1$, or $r \to \infty$, with the functions defined as (note that the coefficients are different from the ones in the horizon expansion)

$$\begin{aligned}
F_1(\rho, x) &= \sum_0^{n_{max}} a_n(x)(1-\rho)^n \\
F_2(\rho, x) &= \sum_0^{n_{max}} b_n(x)(1-\rho)^n \\
F_3(\rho, x) &= \sum_0^{n_{max}} e_n(x)(1-\rho)^n \\
F_4(\rho, x) &= \sum_0^{n_{max}} c_n(x)(1-\rho)^n \\
F_5(\rho, x) &= \sum_0^{n_{max}} f_n(x)(1-\rho)^n \\
F_6(\rho, x) &= \sum_0^{n_{max}} d_n(x)(1-\rho)^n
\end{aligned} \tag{5.53}$$

and inserting them into the equations, we get as solutions conditions on the $a_n,\ b_n,\ c_n,\ d_n,\ e_n,\ f_n$ at infinity. These conditions will be the boundary conditions at $\rho = 1$, and we chose the following

$$\begin{aligned}
a_0 &= \frac{\gamma}{-2+3\gamma} \\
b_0 &= 1 \\
c_0 &= \gamma \\
e_0 &= 0 \\
f_0 &= \gamma \\
&\dots
\end{aligned} \tag{5.54}$$

and $d_0(x)$ is related to the potential at infinity. As we can see, there is a free parameter γ found by relating the metric components at infinity. The parameter γ will be related to the temperature of the black hole, so adjusting

it will allow us to search for different solutions. To see how, consider the exact metric components g_{tt} and $g_{\theta\theta}$ for AdS and the ones given by our ansatz at infinity

$$ds^2 = \frac{r_0^2}{(1-\rho_{phys}^2)^2} dt_{phys}^2 + \frac{r_0^2}{(1-\rho_{phys}^2)^2} d\theta^2 + \dots \tag{5.55}$$

$$ds^2 = \frac{r_0^2}{(1-\rho^2)^2} \frac{\gamma}{3-2\gamma} dt^2 + \gamma \frac{r_0^2}{(1-\rho^2)^2} d\theta^2 + \dots \tag{5.56}$$

Comparing the $g_{\theta\theta}$ components, we can fix the radial coordinate, in the form

$$\frac{\gamma}{(1-\rho^2)^2} = \frac{1}{(1-\rho_{phys}^2)^2} \tag{5.57}$$

and use this to determine how the physical time relates to the time coordinate of our ansatz

$$\frac{r_0^2}{3\gamma-2} dt^2 = r_0^2 dt_{physical}^2 \implies t_{phys} = \frac{t}{\sqrt{3\gamma-2}} \tag{5.58}$$

As we have discussed, the temperature is given by the inverse of the periodicity of the physical time. To check the periodicity we write the metric at $\rho = 0$ as

$$ds^2 = \tilde{f}(0) F_1(0,x) \rho^2 dt^2 + \frac{4r_0^2}{\tilde{f}(0)} F_2(0,x) d\rho^2 \tag{5.59}$$

with, according to 5.33, $a_0 = b_0$, and we introduce a new coordinate $\psi = \sqrt{\frac{4r_0^2}{\tilde{f}(0)}}$, yielding

$$ds^2 = \left(\frac{\tilde{f}(0)}{2r_0} \right)^2 \psi^2 dt^2 + d\psi^2 \tag{5.60}$$

$$t \in 2\pi \frac{2r_0}{\tilde{f}(0)} \tag{5.61}$$

and, finally,

$$\frac{1}{T} = \frac{4\pi}{\tilde{f}(0)} \frac{1}{\sqrt{3\gamma-2}} \tag{5.62}$$

So, adjusting the parameter γ will allow us to search for solutions with different temperatures.

5.4.2 Poles

Although for the simpler cases they aren't necessary, since the solutions will not depend on this coordinate, there will be a need to impose conditions on the boundaries defined by $x = \pm 1$. First, let us note that these conditions should be identical in both poles, since there is in principle nothing that would distinguish them (until we introduce a way to break the symmetry in x). So, we chose to impose smoothness at the poles and that the off-diagonal term vanishes

$$\frac{\partial F_i}{\partial x}|_{x=0,1} = 0 \tag{5.63}$$

$$F_3 = 0 \tag{5.64}$$

One of the reasons we chose this coordinate system is that $x = \frac{1}{2}$ corresponds to the equator, and that will be very useful when we want to compare physical quantities that require values of the functions at these points.

5.4.3 Electromagnetic potential

If we want an electrically charged type of solution, we need to introduce an electromagnetic potential in the problem, and we can do this by setting an appropriate boundary condition. At the horizon, we impose that this potential should vanish, and to see how it behaves at infinity, let us consider, for simplicity, a Schwarzschild solution in anti de Sitter space in usual spherical coordinates.

Now, we will add an electromagnetic potential in the form of a perturbation

$$A(r, \theta) = \delta A(r, \theta) dt \tag{5.65}$$

This potential should solve the Maxwell equation $\nabla^\mu F_{\mu\nu} = 0$, which corresponds to the equation

$$L^2 \cot\theta \partial_\theta \delta A(r,\theta) - (L^2(2M - r) - r^3)(2\partial_r \delta A(r,\theta) + r\partial_r^2 \delta A(r,\theta)) = 0 \tag{5.66}$$

This can be solved by separation of variables, since the θ part of the equation

is a Legendre equation and admits the Legendre polynomials as solutions

$$\delta A(r,\theta) = f_l(r) P_l(\cos\theta) \tag{5.67}$$

Now we solve the equation in r, expanding around $r \to \infty$ since this is where we will impose this condition. We drop the lowest powers in r and

$$-l(l+1)L^2 f_l(r) + r^3(2f_l'(r) + r f_l''(r)) = 0 \tag{5.68}$$

And the solution is

$$f_l(r) = C_1^{(l)} \cos\left(\sqrt{l(l+1)}\frac{L}{r}\right) - C_2^{(l)} \sin\left(\sqrt{l(l+1)}\frac{L}{r}\right) \tag{5.69}$$

or, expanding around $r \to \infty$

$$f_l(r) = C_1^{(l)} - C_2^{(l)}\sqrt{l(l+1)}\frac{L}{r} + O(r^{-2}) \tag{5.70}$$

where the first term (with $l = 0$) corresponds to a potential related to the existence of a total charge, and the second term to the electric field generated by said charge. This can be written as

$$A_t = \Phi(\theta,\phi) + \frac{\rho(\theta,\phi)}{r} + O(r)^{-2} \tag{5.71}$$

where, if we wanted to add an external electric field, we could do it by adding a term to the potential of the form

$$\Phi(\theta,\phi) = \Phi_0 + e\cos\theta \tag{5.72}$$

and this could be set as a boundary condition for F_6 at infinity.

5.5 Spectral method

Now that we have a well posed elliptic boundary value problem for some functions F_i, we can proceed to use the spectral method to determine its

solution, as explained in chapter 2.

First, we discretize the coordinates ρ and x with the use of a Chebyshev grid in each direction, and label it according to 3.11. Then we transform the functions into lists of function values at the determined labeled set of points: $(\rho, x) \to p_k (k = 1, ..., n)$, $F_i(\rho, x) \to f_i(p_k)(i = 1, ..., 6)$; and all the derivatives acting on these functions into Chebyshev matrices acting on the vectors where the function values are stored. In the points that correspond to the boundaries, we substitute the equations for the boundary condition those points must satisfy, that is, in points belonging for example to the boundary $\rho = 1$, instead of the six Einstein-Maxwell harmonic equations, we will have the boundary conditions mentioned in the previous section, imposed as equations of the form: $F_1[p_k] - \frac{\gamma}{-2+3\gamma}$, $F_2[p_k] - 1$, $F_3[p_k]$, $F_{4,5}[p_k] - \gamma$ and $F_6[p_k] - \Phi_0 - e\sqrt{1 - 16x^2(1-x)^2}$ for $k \in \{1, \ldots, n+1\}$ (where Φ_0 is the potential and e is the external electric field).

This method has now reduced our problem to solving a number of equations, one for each point in our grid. These equations may be represented as entries $E_i(f_{1,2,3,4,5,6}, p_k)$, and the values of the functions on the grid are put in the list $f = (f_1[1...N], f_2[1...N], f_3[1...N], f_4[1...N], f_5[1...N], f_6[1...N])$ of length $6N$, and the system is solved by iteration, starting with an initial guess, and then applying Newton's method until convergence is reached. The solution will come as a list f from which we will need to extract the first N elements for f_1, the second N for f_2, and so on.

Depending on the solution we are looking for, we may choose the initial solution accordingly, and even after finding one such solution, we can use it as an initial seed in the search for another more complicated one, which is an efficient way to look for solutions that are initially very far away from our known solutions.

5.6 Results

In this section we will present and discuss some solutions obtained with the use of the methods described, comparing with analytical solutions in the cases where they exist, and computing important physical quantities.

While analyzing the results, some care has to be taken, since they will be in the coordinates fixed by the Einstein-de Turck equations (as explained in chapter 4), so when we compare them with analytical results, we will have to compute from these results physical quantities that are invariant under coordinate transformations.

For simplicity, we will write all temperatures in the text without a factor of $\frac{1}{\pi}$, so $T = 1$ actually means $T = \frac{1}{\pi}$.

5.6.1 Schwarzschild AdS

The Schwarzschild AdS solution is obtained by setting $F_1 = F_2 = F_4 = F_5 = 1$ and $F_3 = F_6 = 0$. In this case there is no charge, so the parameter we will have to tune is T (or, equivalently, γ). Some care has to be taken when dealing with the solution, because, as we have shown in section 5.2.1, it has in this case two branches, or two different values of r_0 for the same temperature. We are interested in working with the stable solution (positive specific heat), so we have to be careful when choosing the reference metric to try and not set it too far away from this solution, otherwise it will possibly flow towards the other one, so we set it exactly at $r_0 = 1$.

Regarding the initial seed, we chose one close to the actual solution we are hoping to find, as a way of checking if the method was working as intended. After obtaining the solution as lists of values for the functions F_i, the question remains as how to present them and compare them with the exact solution. Obviously in this case this is not a problem, since all the F_i are constants, so they do not depend on the coordinates, and the program should just return lists full of ones, which in fact it does. But, preparing for other more complicated cases, we will present an easy and natural way to compare our numerical solution to the exact one, using the metric components (for example $g_{\tau\tau}$ and $g_{\theta\theta}$).

In our ansatz for the metric

$$g_{\tau\tau} = \tilde{f}(\rho)\frac{F_1(\rho, x)\rho^2}{(1-\rho^2)^2} \tag{5.73}$$

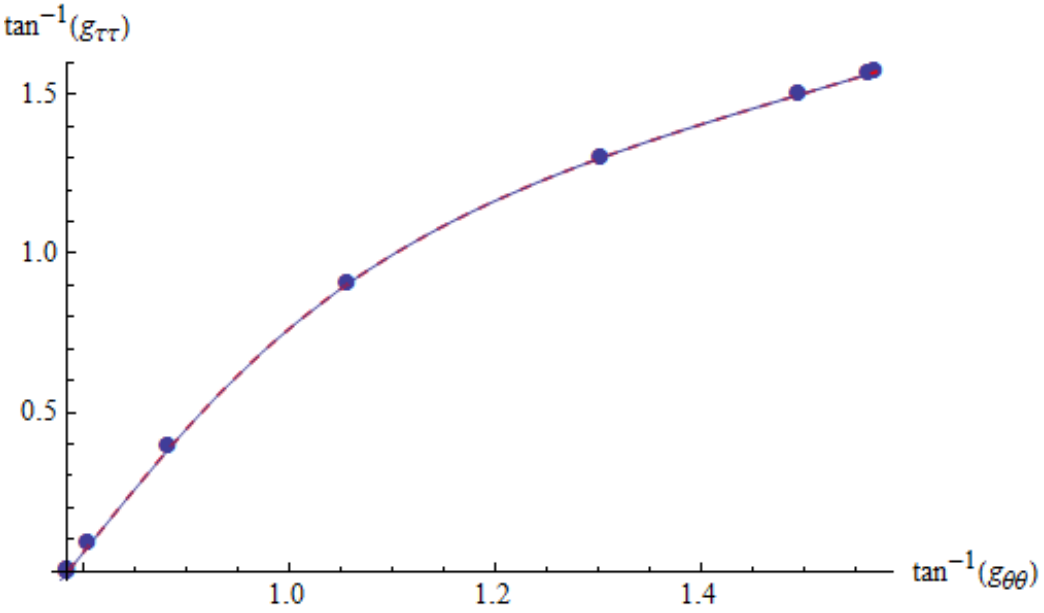

Figure 5.5: $\arctan g_{\theta\theta}$ vs $\arctan g_{\tau\tau}$ for a Schwarzschild black hole with $T = 1$. The solid line represents the exact and the dots represent the numerical solution. The dashed line is the interpolating polynomial (eq. 2.12) of the data points.

$$g_{\theta\theta} = \frac{r_0^2}{(1-\rho^2)^2} F_4(\rho, x) \tag{5.74}$$

Note that in the cases where there is no break in spherical symmetry, the functions $F_i(\rho, x)$ can be written as just $F_i(\rho)$, since they will not show dependence in the coordinate x. For the same reason, $F_3(\rho)$ will vanish everywhere in these cases, and we have not included it in the definition of $g_{\theta\theta}$.

We can now plot these metric components for our solution as well as for the exact case. Since these terms go to infinity with r, we plotted their arctangent so all points on the grid would be in the plot. Figure 5.5 shows this plot for $T = 1$.

We can now use this solution as a seed to try and find another solution with a different choice of parameters. To remain in the Schwarzchild case, we will change the temperature of the solution we are looking for, and set it to $T = 1.25$. As we can see from Figure 5.1, we expect that this will have the effect of increasing r_0 of the black hole, and calculating it again from our solution we see that this is indeed the case, as for this black hole $r_0 \approx 1.43426$. In Figure 5.6 we can see the same arctangent plot as before.

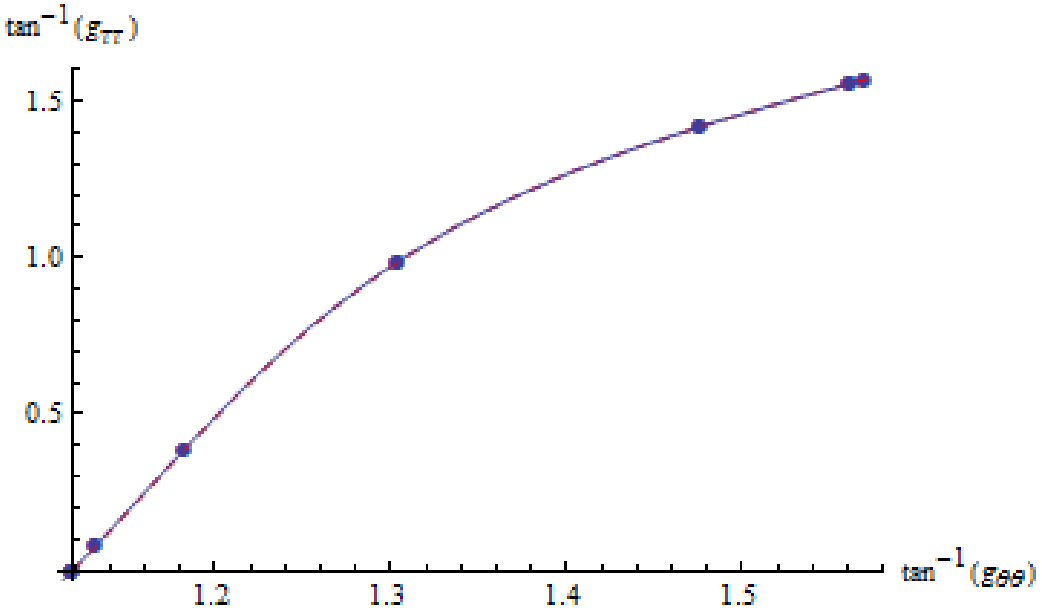

Figure 5.6: arctan $g_{\theta\theta}$ vs arctan $g_{\tau\tau}$ for a Schwarzschild black hole with $T = 1.25$. The solid line represents the exact and the dots represent the numerical solution. The dashed line is the interpolating polynomial (eq. 2.12) of the data points.

By increasing the temperature even further, we can see how the horizon radius increases, and, consequently, the surface area $A = 4\pi r_0^2$, related to the entropy of the black hole given by $S_{BH} = \frac{A}{4}$. Plotting the ratio $\frac{S}{S_0}$, where S_0 is the entropy of the black hole with $T = 1$, we obtain what is shown in Figure 5.7 for the increase in entropy with temperature.

5.6.2 Reissner-Nordstrom AdS

In the case of Reissner-Nordstrom type solutions, we add another parameter to the problem, the potential Φ (or charge Q, related to it by $Q = \Phi r_0$). In Figure 5.8 we plotted $T(r_0)$ for this case, and for $Q = 0.05$ there is once again more than one black hole solution for a given value of T, but as we increase the charge, in the plot to $Q = 0.9$, we can see that the solution becomes unique, but also only exists for the higher value of r_0, so we have to be careful when looking for that solution, an easy way is to start with a low value for the charge and then work our way up, using the last solution as our seed, so we are guaranteed to be iterating in the right direction.

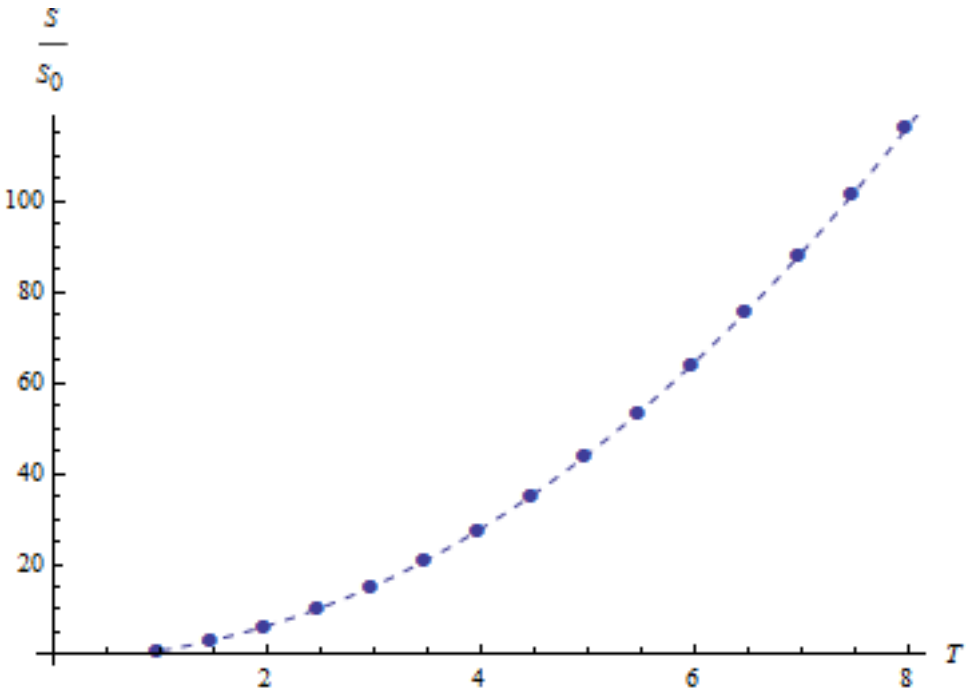

Figure 5.7: Increase in entropy of the black hole with T relative to the $T = 1$ case. The dots represent the numerical results while the dashed line is their interpolating polynomial.

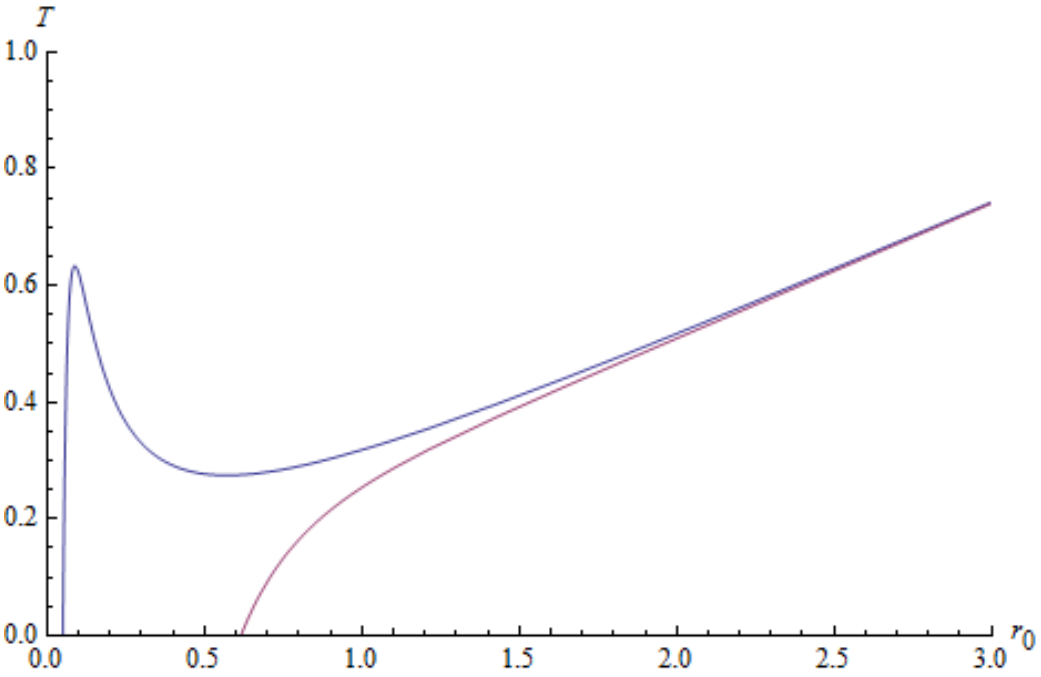

Figure 5.8: Temperature as a function of r_0 for a Reissner-Nordstrom-AdS black hole. Red line represents $Q = 0.05$ and blue line $Q = 0.9$.

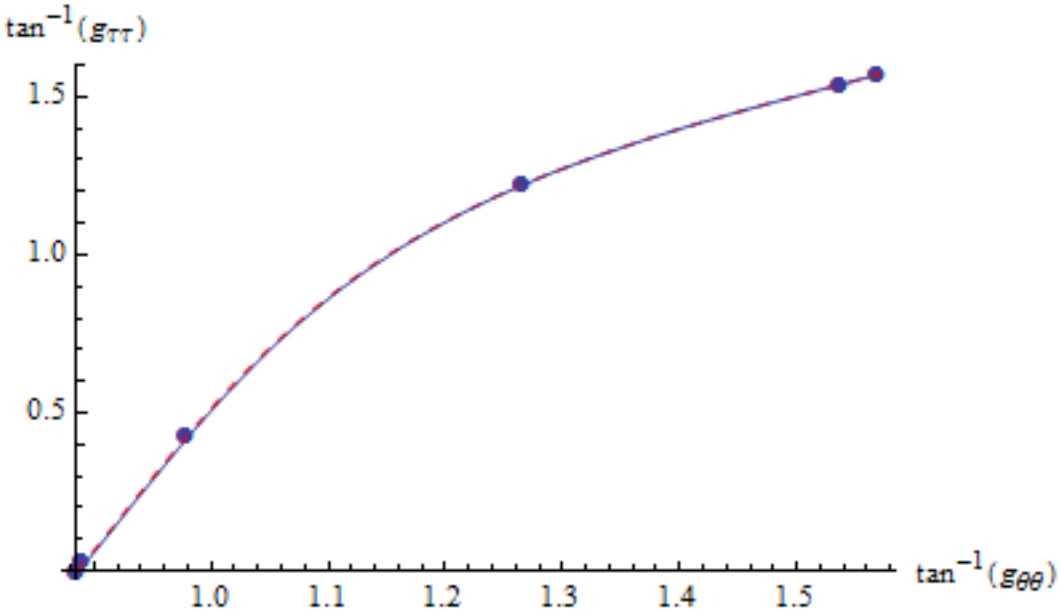

Figure 5.9: $\arctan g_{\theta\theta}$ vs $\arctan g_{\tau\tau}$ for a Reissner-Nordstrom black hole with $T = 1$ and $Q \approx 0.553813$. The solid line represents the exact and the dots represent the numerical solution. The dashed line is the interpolating polynomial (eq. 2.12) of the data points.

Using the standard solution as seed, we introduce a constant Φ potential as a boundary condition at infinity and look for new solutions. With $\Phi = \frac{1}{20}$, we obtain a value for $r_0 \approx 1.00125$, which means the increase in charge leads to an increase in the size of the black hole, as indicated by Figure 5.2. In Figure 5.9 we plot the same arctangent plot of the previous section for the RN case with $\Phi = \frac{1}{2}$.

Again, the resemblance between exact and numerical solution is very high, even with a relatively low number of points. We can play around a bit with the parameters in the phase space of the problem (T, Φ), computing some characteristic features of the black hole such as its surface area or entropy. The geometry of the horizon will however not change using only these parameters, since there is no symmetry breaking in the x (angular) direction.

The surface area is given by

$$A = 2\pi \int_0^1 \sqrt{\frac{16F_4(0,x)}{1+4x(1-x)}} 4x(1-x)\sqrt{F_5(0,x)}\mathrm{d}x \tag{5.75}$$

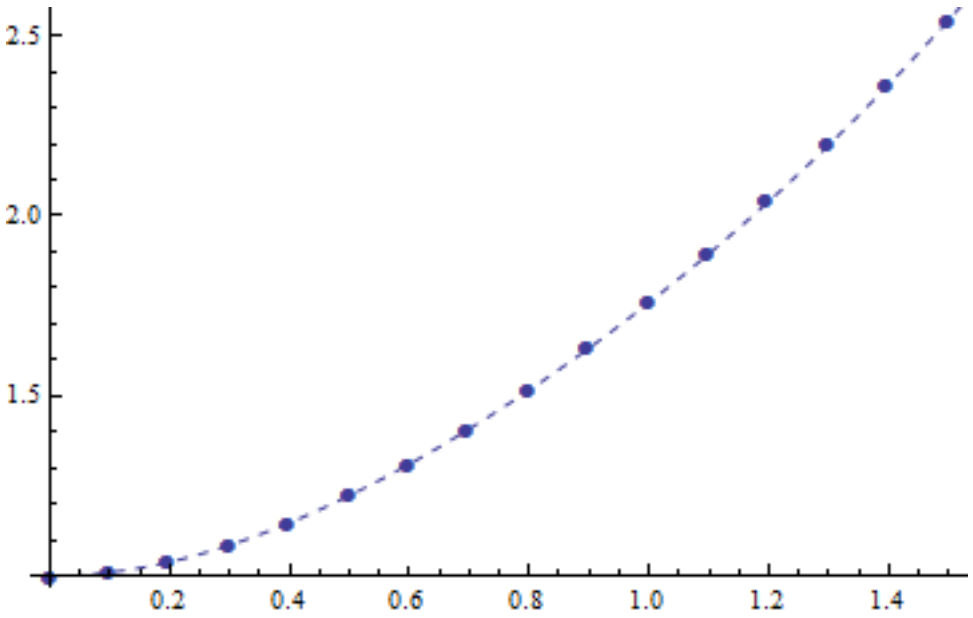

Figure 5.10: Increase in entropy of the black hole with Φ relative to the Schwarzschild case ($\Phi = 0$). The dots represent the numerical results while the dashed line is their interpolating polynomial.

so in the Schwarzschild case, with $F_4 = F_5 = 1$, this amounts to $A = 4\pi$. In figure 5.9 we plot the increase in the surface area with Φ in the range $[0,\ 1.5]$. The behaviour is in agreement with the exact solution presented in Figure 5.2.

5.6.3 Polarizing

We will now introduce a polarization at infinity with an electromagnetic potential dependent on the coordinate x, as described in section 5.4.3. This will have the effect of breaking the spherical symmetry of the problem, leading the charges of the same signal to aggregate in one of the sides of the black hole (if it is electrically neutral, it will still display a symmetry in relation to $x = \frac{1}{2}$). This will have effects on the shape of the horizon, leading to deformations in its geometry, the two poles of the black hole will start to be pulled towards infinity, being connected by an increasingly thin tube, up to a value of the applied electric field $e_{breakdown}$ where this tube will break, forming two separate black holes. The cause of this effect, however, lies beyond the scope of this project, and we will only attempt to determine the value of e

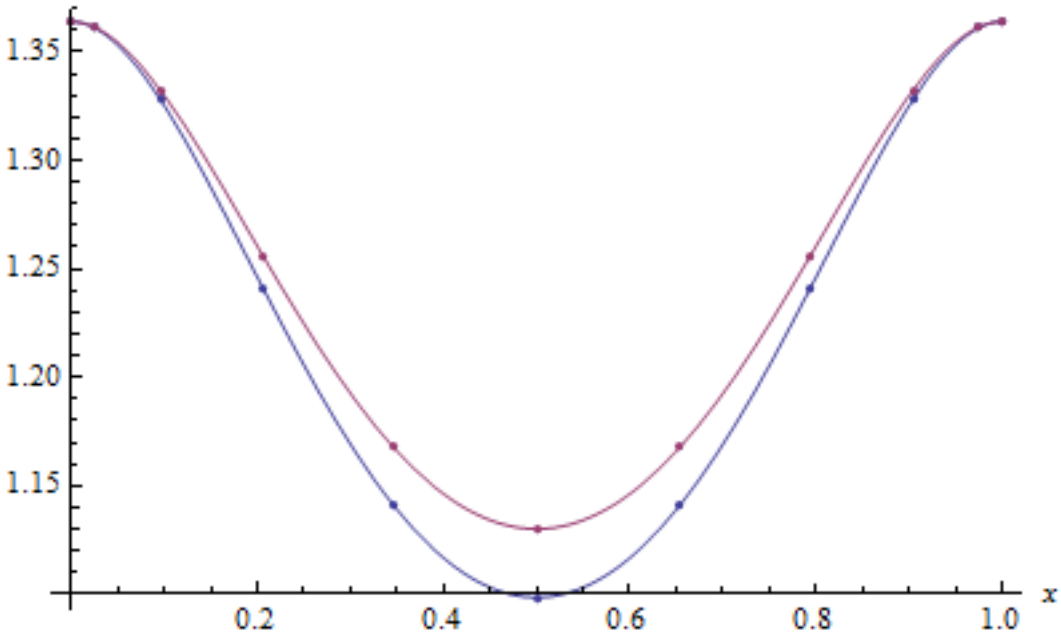

Figure 5.11: Functions $F_4(0,x)$ (blue) and $F_5(0,x)$ (red) as a function of x for a black hole with $T = 1$ and an applied electric field $e = 1$.

for which this happens at a range of temperatures.

Starting with the usual Schwarzschild AdS solution, we will introduce a small electric field and see how the solution behaves, studying the geometry of deformed horizon, the entropy of the black hole and the charge density at infinity.

With $e = 1$, we can already see the break in spherical symmetry by analyzing the functions F_4 and F_5 at the horizon, which are equal in the metric of a 2-sphere $d\Omega_2$. In Figure 5.11 we can see both these functions plotted, and they start to exhibit some differences, which did not happen in any of the previous cases.

The geometry of the horizon itself is not noticeably deformed by this, since the values are small, but it is a good indication that changes will be apparent once we increase the external electric field. The horizon radius does also change and the surface area is approximately 1.1925 that of the Schwarzschild solution.

To determine the charge density at infinity and at the horizon we need to

take some time to study the function $F_6(\rho, x)$ near $\rho = 1$. The electromagnetic potential is given by

$$A = \frac{\rho^2}{r_0} F_6 \mathrm{d}t \tag{5.76}$$

and we will expand F_6 like in equation 5.53 as

$$F_6 = d_0 + (1-\rho)d_1 + O(1-\rho)^2 \tag{5.77}$$

The electromagnetic field strength tensor is then

$$F = \mathrm{d}A = \frac{\rho}{r_0}(2d_0 - 3\rho d_1)\mathrm{d}\rho \wedge \mathrm{d}t \tag{5.78}$$

If we consider

$$Q = \int_{S^2} \star F d\Omega_2^2 \tag{5.79}$$

to be the total charge, we can write it as

$$Q = \frac{1}{4\pi} \int_{S^2} Q(\rho, x) \frac{16(1-x)x}{\sqrt{1+4x-4x^2}} dx d\phi \tag{5.80}$$

where $Q(\theta, \phi)$ is the charge density. Since

$$F \wedge \star F = F^2 \sqrt{g}\ d\rho \wedge dt \wedge dx \wedge d\phi \tag{5.81}$$

where

$$F^2 = 2F_{t\rho} F t \rho g^{tt} g^{\rho\rho} \tag{5.82}$$

and solving for the charge density at infinity

$$Q(\rho = 1, x) = (2F_6(1, x) - 3F_6'(1, x))\sqrt{\frac{F_4 F_5}{F_1 F_2}} \tag{5.83}$$

Using exactly the same method, we obtain the formula for the charge density at the surface of the black hole

$$Q(\rho = 0, x) = 2F_6(0, x)\sqrt{\frac{F_4 F_5}{F_1 F_2}} \tag{5.84}$$

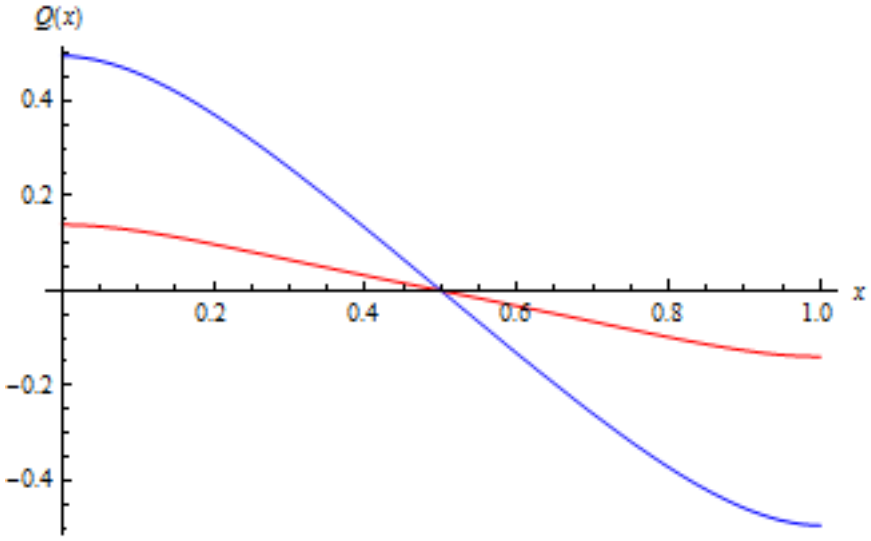

Figure 5.12: Charge density on the sphere at infinity (blue) and on the horizon (red) for applied electric field $e = 1$.

We determine F_6 at infinity and at the horizon through the interpolation function 2.12 and proceed to plot the charge densities in Figure 5.12. We can see that the distributions are similar, although the total flux of the electric field through the sphere at infinity is obviously higher at infinity.

The phase space of the problem has three dimensions, (T, Φ, e), but we only have exact solutions to compare our solutions with in the plane $e = 0$, so the best approach to studying polarized black holes with different temperatures is to first determine the solution to the black hole of the same temperature without any external electric field and then from that solution, using it as an initial guess, search for the new solution we want. There is also the question of how the addition of a $\Phi \neq 0$ will affect the solution, but for now we will increase the value of e for a black hole with $T = 1$, $\Phi = 0$ and see how far we can go, and what effects that produces on the black hole's structure.

We have to work with a few more points now, since we need more precision to reach higher values of external electric field, so we will be working with a grid of $N = 11^2 = 121$ points. We will increase e slowly, using each solution as a seed for the next, to optimize the computational times and minimize numerical errors. Starting with what we have so far for a smaller grid, up

to $e = 1$, we can use our interpolation polynomials for the functions f_i to determine its values in the extra points we have in the bigger grid, avoiding the need to solve the problem with these values again.

The same effects that start to appear when we add an external electric field are reinforced by the increase in its value. In Figure 5.13 there is a plot of an embedding of the horizon of a black hole with $e = 4$ into R^2 along with the standard $e = 0$ case for comparison. The embedding is done considering the following metric for a deformed 2-sphere

$$ds^2 = F^2(\theta)^2 d\theta^2 + G^2(\theta) d\phi^2 \tag{5.85}$$

and, as we know, the flat metric in cylindrical coordinates can be written as

$$ds^2 = dZ^2 + dR^2 + R^2 d\phi^2 \tag{5.86}$$

so, the induced metric on a surface $Z(\theta), R(\theta)$ is given by

$$ds^2 = (Z'^2(\theta) + R'^2(\theta)) d\theta^2 + R^2(\theta) d\phi^2 \tag{5.87}$$

where primes denote derivatives with respect to θ. Equating 5.87 and 5.89 we get

$$R = G \tag{5.88}$$

$$Z'^2 + R'^2 = F^2 \tag{5.89}$$

which implies

$$Z(\theta) = \int_0^\theta \sqrt{F^2 - G'^2} d\theta \tag{5.90}$$

and these functions $Z(\theta), R(\theta)$ can be used to create a 2D plot of a slice of the black hole surface.

As we predicted, the black hole starts to spread out, with charges of opposite signal clustering in its sides. This is very clearly seen in the 3D representation in Figure 5.14, where we can really see the black hole being pulled to the poles where the potential is at its highest value. The surface area of this black hole is approximately 4.89046 times that of the Schwarzschild

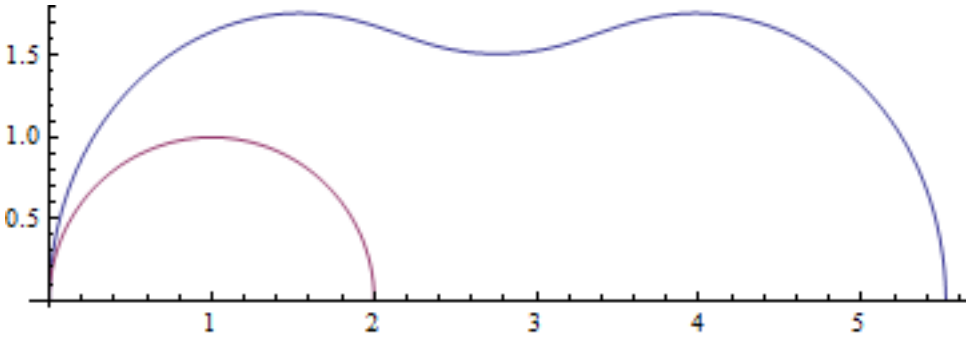

Figure 5.13: Isometric embedding in R^2 of a section of a $T = 1$ black hole surface with an applied electric field of $e = 5$.

case.

Regarding the charge density at infinity and at the horizon in this case, we can see in Figure 5.15 that they differ from the previous case, where they were approximately cosine distributions, now showing a behaviour consistent with the appearance of higher order perturbations in the form of the Legendre polynomials discussed in section 5.4.3.

One interesting aspect of the black hole is the amount of charge present in each of the two lobes as the external electric field is increased, labelled $Q_N = -Q_S$. To compute this, we integrate the flux of the electric field at the horizon given by 5.86 in equation 5.82 for only half sphere (from $x = 0$ to $x = \frac{1}{2}$), obtaining the evolution with e plotted in Figure 5.16.

We can do the same thing for the flux of the electric field at infinity $Q_N^\infty = -Q_S^\infty$, calculated for a section between $x = 0$ and $x = \frac{1}{2}$, and the results are plotted in Figure 5.17.

The solutions start becoming more numerically unstable and take a significant greater computational time to achieve when we approach a particular value of e, where a solution ceases to exist for the discrete case, which we term $e^{(n)}_{breakdown}$, dependent on the number of points on the grid $N = (n+1)^2$. This could mean one of two things, either this value will saturate as $n \to \infty$ and we will get a measure for the true $e_{bd} = e^{(\infty)}_{breakdown}$ for each increase in the number of points, or it will increase without bound, indicating that the solution still exists in the continuum case for arbitrarily large e. The fact that the growth in $e^{(n)}_{breakdown}$ is smaller for each increment in n, as shown in

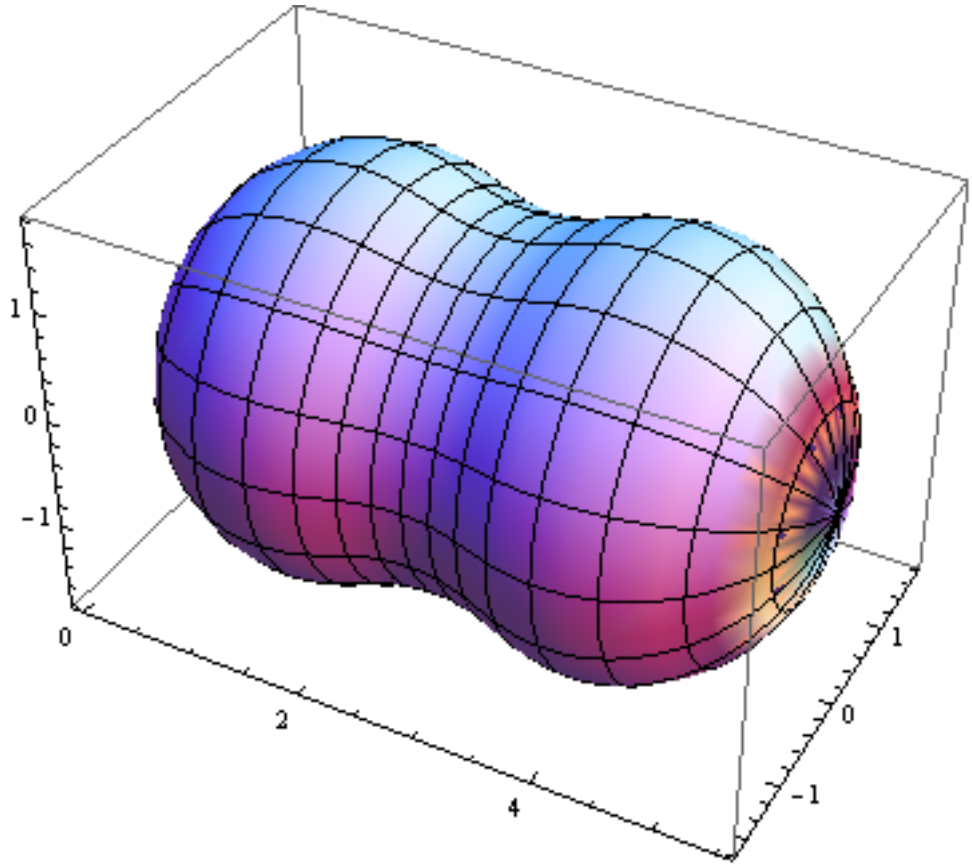

Figure 5.14: Isometric embedding in R^3 of a $T = 1$ black hole horizon with an applied electric field of $e = 5$.

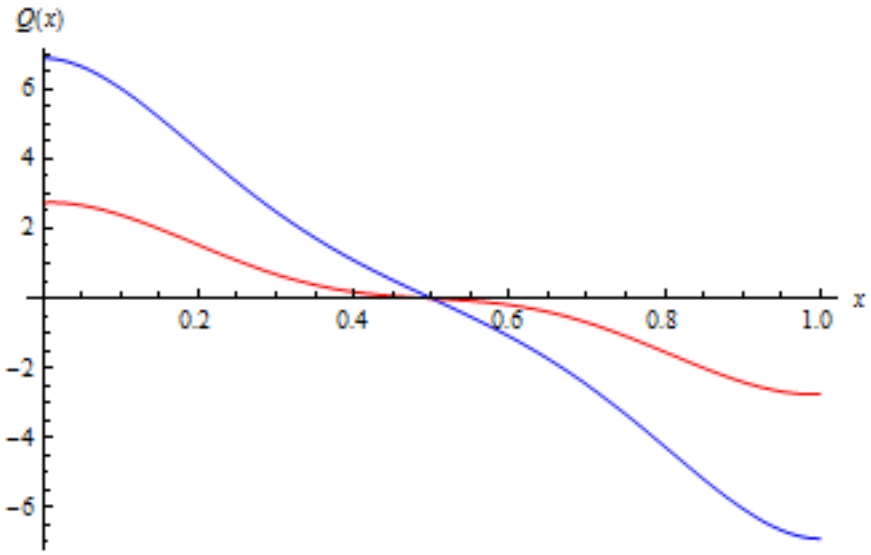

Figure 5.15: Charge density on the sphere at infinity (blue) and on the horizon (red) for applied electric field $e = 5$.

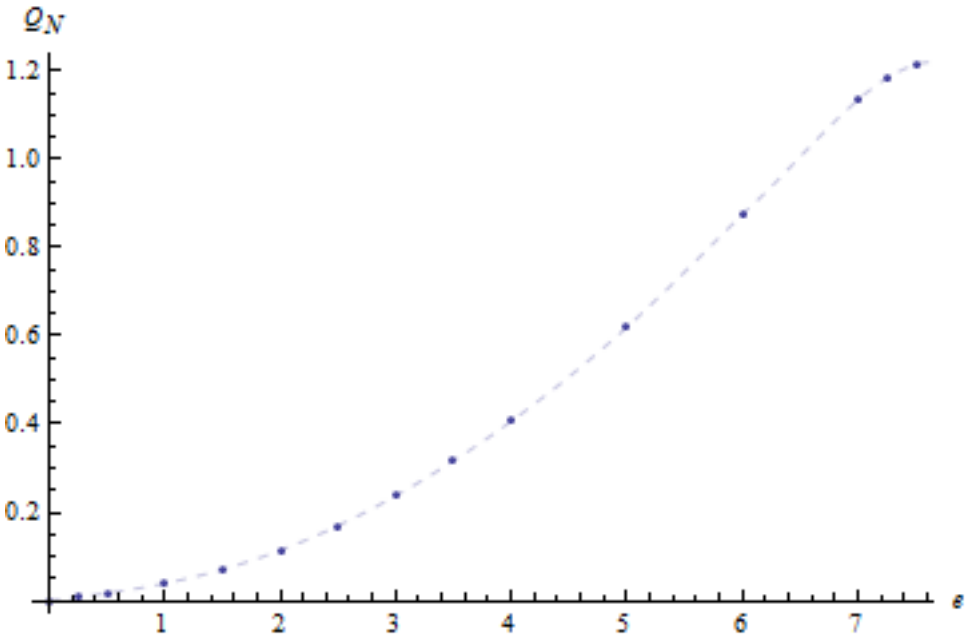

Figure 5.16: Total charge on one of the lobes, Q_N, as a function of e.

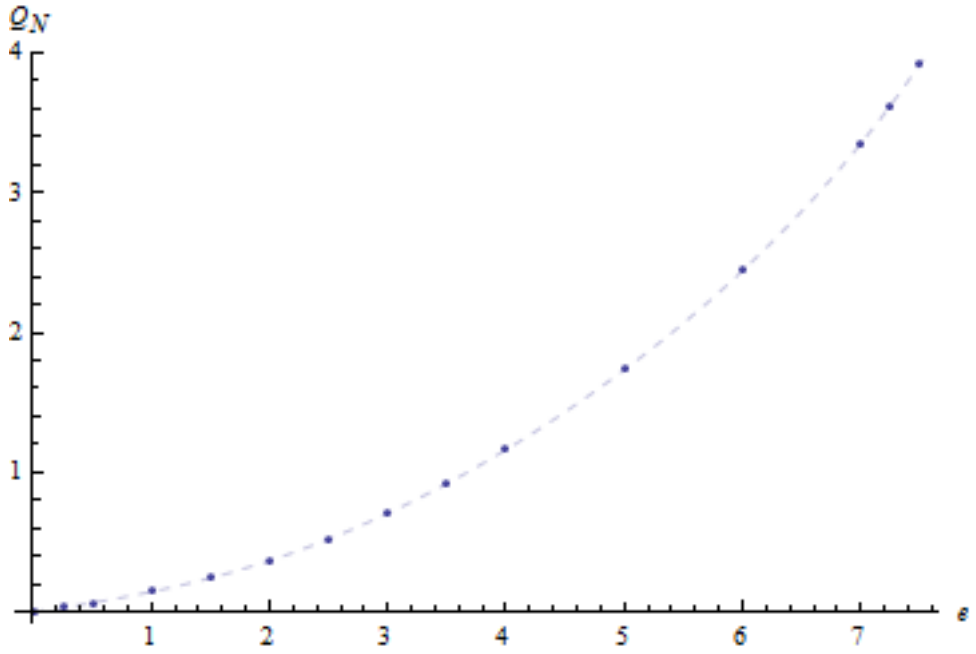

Figure 5.17: Flux of the electric field through half the sphere at infinity Q_N^{∞} as a function of e.

the logarithmic plot of Figure 5.18, could indicate that the former is correct, but it will take a lot more computational power to know this with relative certainty.

Plotted in Figure 5.19 is the black hole horizon for $e = 8$, we can see that the poles are becoming far greater than the middle tube, which could be an indication of its tendency to break for any increase in applied electric field.

Another black hole feature we will analyze is its entropy in relation to the Schwarzschild case, as was done in Figure 5.10 for the case of electrically charged universes. In Figure 5.20 the same kind of plot is shown, now as a function of applied electric field e, as we can see the behaviour is similar with a smaller growing rate with the electric field than with the potential Φ.

One of the effects of increasing the temperature is to increase the size of the black hole, like we pictured on Figures 5.1 and 5.2. In the case of polarized black holes it works in the same way, but since the numerics are more complex it starts to become less feasible to reach values of e close to the breakdown value for n less than 11. However, the behaviour at small e, which we portray in Figure 5.21, indicates that the effects of e are more pronounced

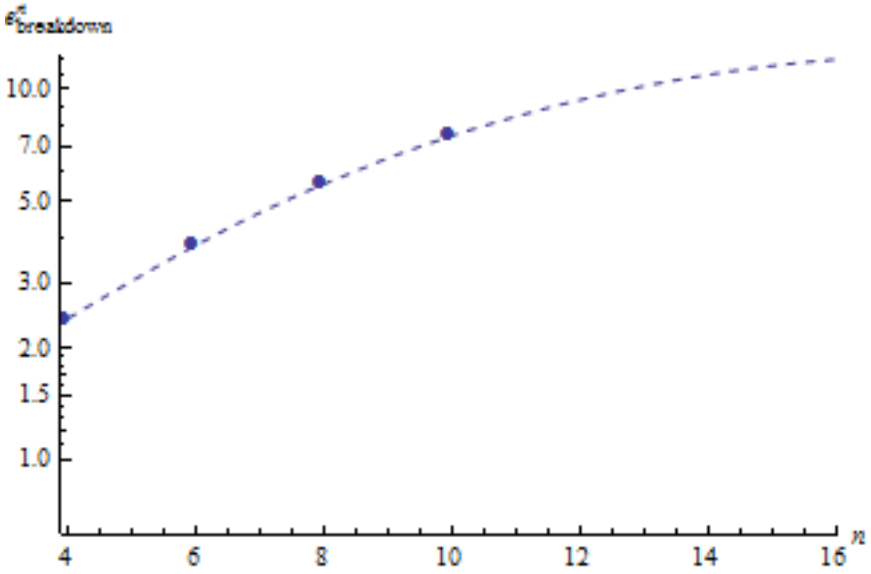

Figure 5.18: Interpolation of $e^{(n)}_{breakdown}$ as a function of n.

(in terms of the flattening of the horizon) for higher T. Interpolating this to larger applied electrical fields, it probably means that the breakdown value of e will decrease for increasing temperature.

In terms of the potential Φ, we predicted that its effects would be to break the existing symmetry of the problem with respect to $x = \frac{1}{2}$, and we can see in Figure 5.22 that this is the case, where the right lobe is getting significantly smaller than the left with the increase in Φ. We can also see this by analyzing the asymmetry of the charge densities at infinity or at the horizon, in Figure 5.23. Further analysis for higher values of the potential is prevented by the same computational problem, it takes a larger grid to compute the solutions, and it is impractical with our computational resources.

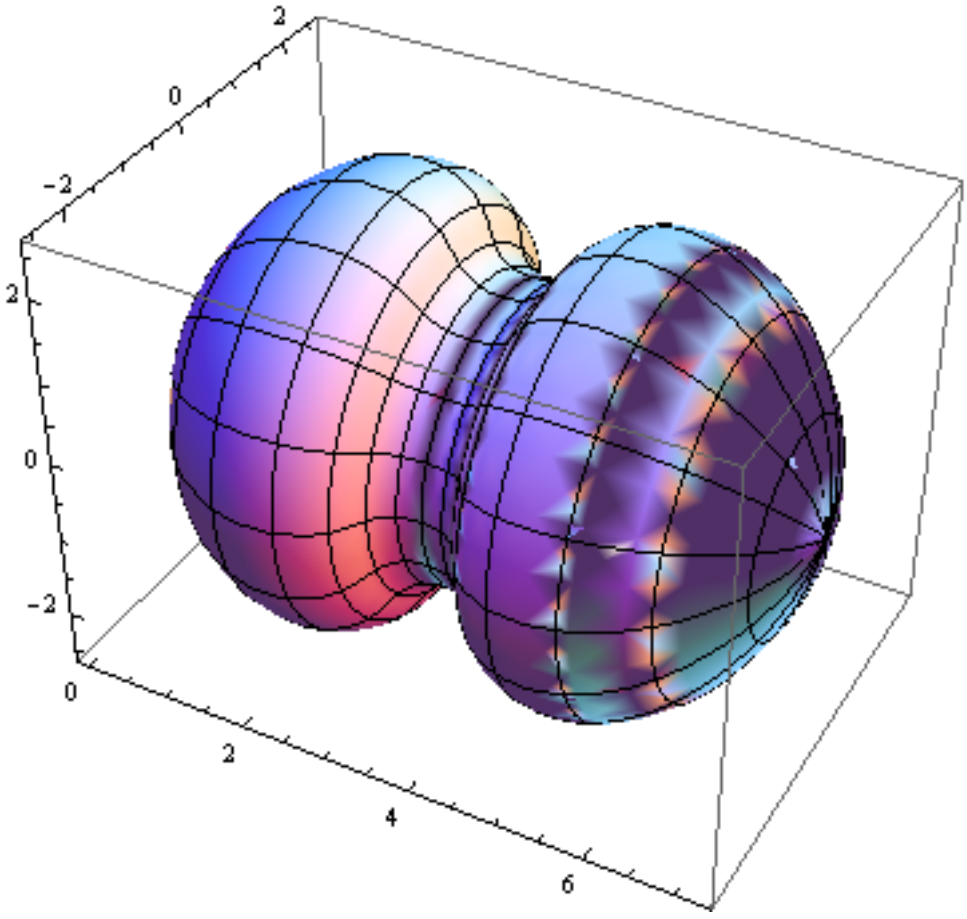

Figure 5.19: Isometric embedding in R^3 of a $T = 1$ black hole horizon with an applied electric field of $e = 8$.

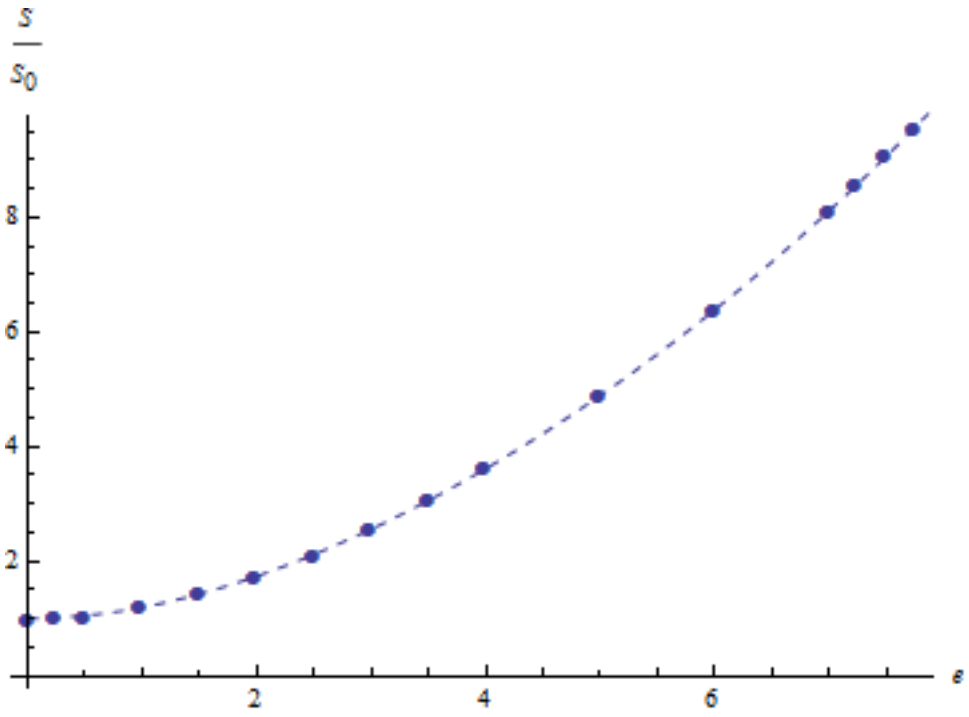

Figure 5.20: Increase in entropy of the black hole with e relative to the Schwarzschild case ($e = 0$). The dots represent the numerical results while the dashed line is their interpolating polynomial.

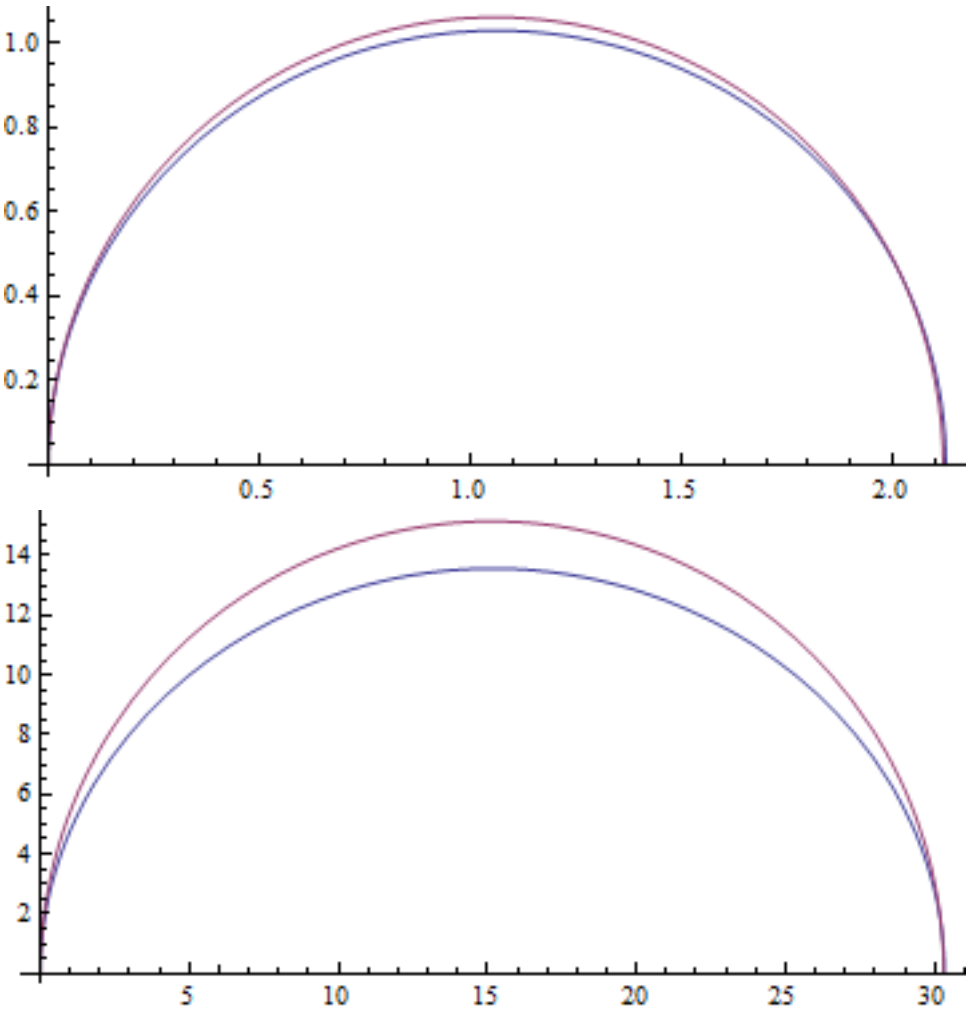

Figure 5.21: Sections of a $T = 1$ (up) and $T = 10$ (down) black hole surface with an applied electric field of $e = 0.64$.

Figure 5.22: Section of a $T = 1$, $\Phi = 1.5$ black hole surface with an applied electric field of $e = 3$.

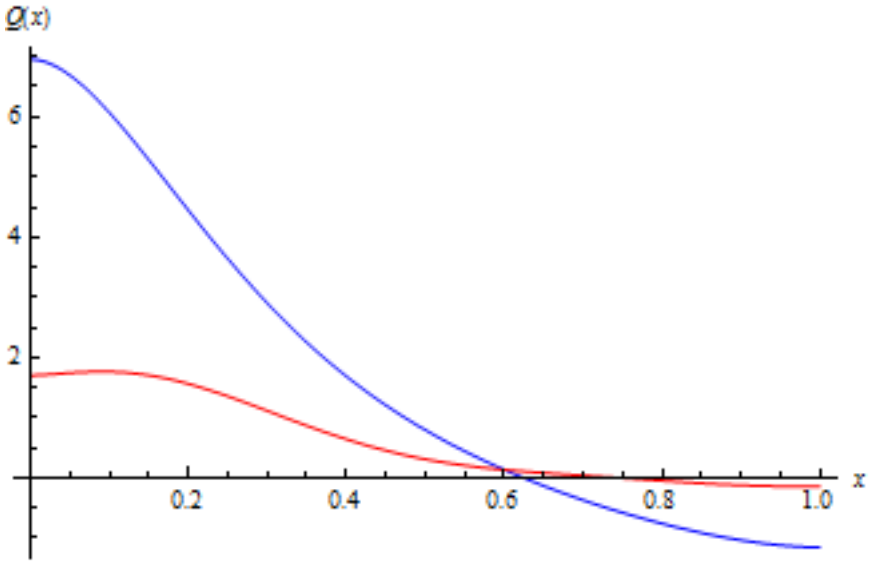

Figure 5.23: Charge density on the sphere at infinity (blue) and on the horizon (red) for applied electric field $e = 5$ on a charged black hole with potential at infinity $\Phi = 1.5$.

Chapter 6

Conclusions

Throughout this thesis we have used spectral methods to solve several types of problems, both mathematical and physical. We tested the convergence properties of these methods, as well as their accuracy in the cases where we had analytical solutions to compare with. We started by introducing spectral methods, providing a formal definition and simple mathematical examples, and then applied them to a well known problem in physics, the steady flow of a viscous fluid past a cylinder, comparing the results obtained with existing numerical simulations to a good match.

We proceeded to the main objective of this work, which was to apply these methods to the Einstein-Maxwell equations of general relativity in AdS space, introducing first the harmonic Einstein equation, a necessary step to make the problem a well defined elliptic boundary value problem. In the final chapter we introduced exact solutions and suitable boundary conditions for this problem, and we started by testing the method, comparing the spherically symmetric solutions obtained to exact solutions, and obtaining very good results for a wide range of parameters. Then, we were able to find several solutions for the case of a Schwarzschild-AdS black hole with an external electric field applied, and they were in agreement with our prediction that it would pull the edges of the black hole, clustering charges of the same sign in its sides and leaving an increasingly thin tube connecting the two. We have found that there is a value for e, dependent on the number of points in

the grid n, which determines where a solution to the discretized equations ceases to exist, and this value will either saturate as $n \to \infty$ to a value of $e_{breakdown}$ in the real (continuum) case, or grow boundlessly with n, indicating that the solution can exist in the continuum for any value of e (although not thermodynamically stable). If the value of applied electric field $e_{breakdown}$ exists, it could correspond to the break of the aforementioned tube, causing the formation of two oppositely charged black holes. We can also look at the plot of the total charge in one side of the black hole $Q_N(e) = -Q_S(e)$ in Figure 5.17, and assume it will saturate for a given value of e, which is consistent with this scenario, where this terminal value is the total charge $|Q|$ of each of the two black holes formed.

We tested some thermodynamical aspects of the deformed black holes, such as their temperature and entropy, and saw that they display the same qualitative behaviour as in the standard $e = 0$ case. The horizon radius scales with the temperature, as opposed to the flat space solution where an increase in temperature will decrease the size of the black hole. The surface, besides getting deformed, has its area increasing with the applied electric field, and consequently the entropy of the black hole also increases. The value for $e_{breakdown}$ is also a function of the temperature, and we predicted it would decrease as the temperature increases, since the changes to the structure of the horizon are more drastic for a higher temperature using the same value of e. Regarding the discussion of 5.2.1 about the Hawking-Page transition for Schwarzschild-AdS black holes, we think a transition of the same type should occur for some values of applied field e, but we were not able to determine it using our formalism. We conjecture that it will behave in a way somewhat similar to the one presented in Figure 5.24, which is a phase space plot of the black hole states in the $\Phi = 0$ plane. In this plane, there are three possible phases, a phase where the existence of the black hole is not energetically favourable, at $T < T_c$, one where the black hole exists and, for $e > 0$, is deformed, and other where, for values of e larger than $e_{breakdown}(T)$, we expect there will be two separate and oppositely charged black holes.

It is possible to perform the same analysis for a case with $\Phi \neq 0$ being

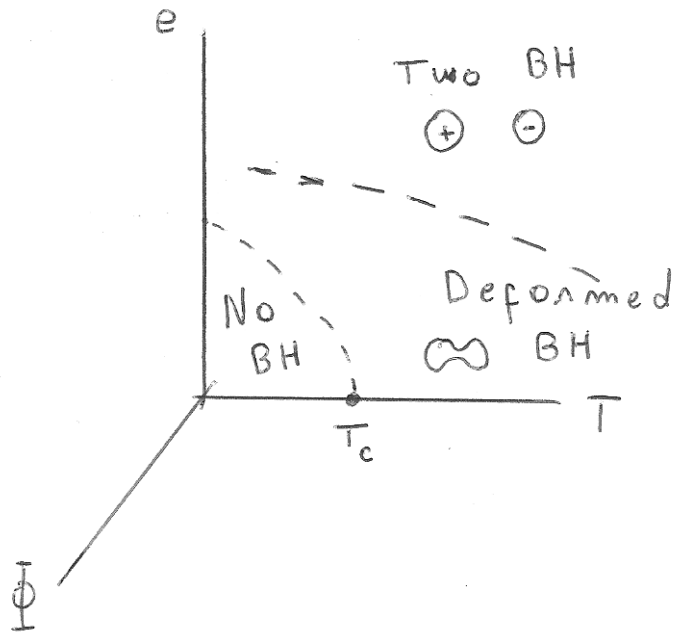

Figure 6.1: Phase diagram of the system in the plane $\Phi = 0$ of the phase space (T, Φ, e).

the potential at infinity that will create a charged black hole. In the plane $e = 0$ there are analytic solutions [6], while if we apply an electric field e the deformed black hole will be asymmetric, as we have shown in Figure 6.1, and it is possible in principle to determine the dependence of the parameters T_c and $e_{breakdown}$ on the potential.

This is obviously a highly speculative plot, and future work will be directed at obtaining actual results that could help determine its specific form and the character of the phase transitions. We need more computational power to obtain solutions in larger grids and with a wider range of parameters.

Finally, as a test of the strength and convergence power of the method used, we compared the solutions obtained for different values of n using the same properties, taking the solutions for $n = 10$ (the highest value we were able to attain using the available computational resources) as a basis for comparing the solutions obtained with different n, so the error is estimated in relation to those solutions, by taking the interpolating polynomial for each

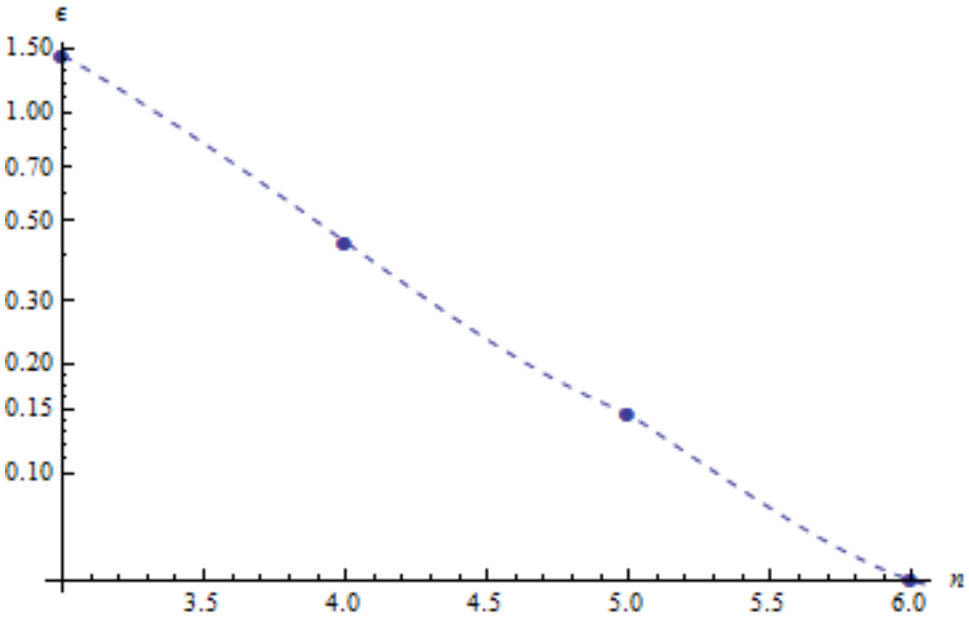

Figure 6.2: Logarithmic plot of the error err_n of solution with respect to $n = 10$ solution as a function of n.

of the F_i and computing

$$err_n = \sqrt{\sum_{i=1}^{6} \max_{0\leq\rho,x\leq 1} |F_i^{(10)}(\rho, x) - F_i^{(n)}(\rho, x)|^2} \tag{6.1}$$

We used as an example a solution where we had $T = 1$ and $e = 1$. The results are shown in Figure 6.2. As we can see, the convergence of the method with number of points is approximately exponential in this case, showing once again the strength of this method, even when working with a set of highly complex equations such as the Einstein equations, and with limited computational resources. Also, even for n as low as 6, the solutions already display a remarkable precision, with a total error $err_6 \approx 10^{-2}$. All of this goes to show why spectral methods are one of the most compelling methods to tackle numerical problems in a lot of areas of physics, amongst them general relativity.

Bibliography

[1] D. Aliev, A.;Gal'tsov. Exact solutions for magnetized black holes. *Astrophys. Space Sci.*, (155), 1988.

[2] S. Ammineborg. Making anti-de sitter black holes. *arXiv*, (gr-qc/9604005), 1996.

[3] M. Astorino. Charging axisymetric spacetimes with cosmological constant. *JHEP*, (86), 2012.

[4] A. Ballon-Bayona. Holographic deconfinement transition in the presence of a magnetic field. *arXiv*, (hep-th/13076498v2), 2013.

[5] Banerjee;Modak;Roychowdhury. Thermodynamics of hawking-page phase transition in ads black holes. *arXiv*, (gr-qc/11063807v1), 2011.

[6] Banerjee;Modak;Roychowdhury. A unified picture of phase transitions: from liquid vapour systems to ads black holes. *arXiv*, (gr-qc/11063877v3), 2012.

[7] M. Bondarescu. Isometric embedding of black hole horizons in three dimensional flat space. *arXiv*, (gr-qc/0109093v3), 2006.

[8] John P. Boyd. *Chebyshev and Fourier Spectral Methods*. Dover Publications, 2000.

[9] J. Brill, D.; Louko. Thermodynamics of (3+1)-dimensional black holes with toroidal or higher genus horizons. *arXiv*, (gr-qc/9705012v2), 1976.

[10] David Brown. Black hole thermodynamics in a box. (gr-qc/9404006v1), 1994.

[11] S. Carlip, S.; Vaidya. Phase transitions and critical behavior for charged black holes. *arXiv*, (gr-qc/0306054v1), 2003.

[12] P. Catalano. Numerical simulation of the flow around a circular cylinder. *International Journal of Heat and Fluid Flow*, (24), 2003.

[13] Peter Constantin. *Navier-Stokes equations.* Chicago Lectures in Mathematics, 1988.

[14] F. Ernst. Black holes in a magnetic universe. *J. Math. Phys.*, (17), 1976.

[15] B. Fornber. A numerical study of steady viscous flow past a circular cylinder. *J. Fluid Mech.*, (98), 1980.

[16] E. Fraga. Large nc deconfinement transition in the presence of a magnetic field. *arXiv*, (hep-th/12077094v2), 2013.

[17] S. Gibbons, G.; Hawking. Action integrals and partition functions in quantum gravity. *Physical Review D*, (10), 1976.

[18] A. Gil. *Numerical Methods for Special Functions*, chapter Chebyshev Expansions. SIAM, 2007.

[19] A. Gould. Derivation of black hole entropy. *SLAC - PUB*, (4061), 1996.

[20] B. Gouteraux. Black hole solutions to einsteins equations in the presence of matter and modifications of gravitation in extra dimensions. *arXiv*, (hep-th/10114941v1), 2010.

[21] J. Griffiths. *Exact Space-Times in Einstein's General Relativity.* Cambridge University Press.

[22] D. Hawking, S.; Page. Thermodynamics of black holes in anti-de sitter space. *Commun. Math. Phys.*, 87(577-588), 1983.

[23] T. Headrick, M.;Wiseman. A new approach to static numerical relativity, and its application to kk black holes. *arXiv*, (gr-qc/09051822v2), 2009.

[24] Parthasarathi Majumdar. Generalized hawking-page phase transition. *arXiv*, (gr-qc/0701014v1), 2007.

[25] J. Maldacena. The gauge/gravity duality. *arXiv*, (gr-qc/11066073v1), 2011.

[26] J. Peca, C.; Lemos. Thermodynamics of reissner-nordstrom-anti-de sitter black holes in the grand canonical ensemble. *arXiv*, (gr-qc/9805004v3), 2000.

[27] Jorge Santos. Chapter 2: Numerical approach (unpublished).

[28] N. Trefethen. *Finite Difference and Spectral Methods for Ordinary and Partial Differential Equations*, chapter Chebyshev spectral methods. Unpublished, 1996.

[29] R.M. Wald. *General Relativity*. The University of Chicago Press, 1984.

[30] R. Wild, W.; Kerns. Surface geometry of a black hole in a magnetic field. *Physical Review D*, (2), 1980.

[31] T. Wiseman. Numerical construction of static and stationary black holes. (gr-qc/1107.5513v1), 2011.

[32] E. Witten. Anti-de sitter space, thermal phase transition, and confinement in gauge theories. *arXiv*, (hep-th/9803131v2), 1998.

[33] P. Zhao. Black holes in anti-de sitter spacetime.

List of Figures